NASA Technical Memorandum 100953

Experimental Determination of Aerodynamic Damping in a Three-Stage Transonic Axial-Flow Compressor

Frederick A. Newman
Lewis Research Center
Cleveland, Ohio

August 1988

NASA

EXPERIMENTAL DETERMINATION OF AERODYNAMIC DAMPING IN A THREE-STAGE TRANSONIC AXIAL-FLOW COMPRESSOR

Frederick A. Newman
National Aeronautics and Space Administration
Lewis Research Center
Cleveland, Ohio 44135

ABSTRACT

Rotor blade aerodynamic damping is experimentally determined in a three-stage transonic axial flow compressor having design aerodynamic performance goals of 4.5:1 pressure ratio and 65.5 lbm/sec weight flow. The combined damping associated with each mode is determined by a least squares fit of a single degree of freedom system transfer function to the nonscynchronous portion of the rotor blade strain gage output power spectra. The combined damping consists of the aerodynamic damping and the structural and mechanical damping. The aerodynamic damping varies linearly with the inlet total pressure for a given equivalent speed, equivalent mass flow and pressure ratio while the structural and mechanical damping is assumed to be constant. The combined damping is determined at three inlet total pressure levels to obtain the aerodynamic damping. The third stage rotor blade aerodynamic damping is presented and discussed for 70, 80, 90, and 100 percent design equivalent speed. The compressor overall performance and

TABLE OF CONTENTS

SYMBOLS

A	area, also rotating data system gain
a	distance of elastic axis rearward of center of gravity of typical section
B_e	resolution bandwidth
B_r	half power point bandwidth
b	semichord
C(k)	Theodorsen's function
c	damping coefficient, also constant
C_p	specific heat at constant pressure
E	Young's Modulus
e_b	normalized power spectrum bias error
e_r	normalized power spectrum random error
F	force
F(K)	real part Theodorsen's function
f	frequency
f_n	undamped natural frequency
G	gage factor
G_{xx}	power spectrum of input x
G_{yy}	power spectrum of output y
G(k)	imaginary part of Theodorsen's function
g	conversion constant 32.17 lbm ft/lbf sec
H	total enthalpy, also frequency response function
h	bending displacement
I	electric current, also mass moment of inertia

i	$\sqrt{-1}$, index
$\bar{i}$	unit vector
J	conversion coefficient 778 ft lbf/Btu
j	index
k	spring constant, also reduced frequency
L	unsteady lift
M	moment, also unsteady aerodynamic moment, Mach number
m	section mass per unit width
$\dot{m}$	mass flow rate
N	rotative speed, percent of 16,042 desigr. rpm
n	total number
P	total pressure, also bending excitation
p	static pressure
Q	torsion excitation moment
q	dynamic pressure
R	electric resistance, also gas constant for air
r	error in least squares procedure
$\bar{r}_a$	displacement vector from elastic axis to center of gravity
$\bar{r}_{cg}$	displacement of center of gravity
T	total temperature
t	time, also static temperature
U	fluid velocity relative to blade or section
x	input coordinate
y	output coordinate
α	torsion displacement

γ ratio of specific heats

Δ recovery-correction factor

δ ratio of inlet total pressure to standard pressure of 14.7 psia

ϵ strain

ζ damping ratio

η_{ad} adiabatic efficiency

θ ratio of inlet total temperature to standard temperature of 518.7 R

μ mass ratio

ρ density

τ non-dimensional time

Φ Wagner's function

ω radian frequency

ω_h undamped natural frequency in bending

Subscripts

a aerodynamic, also arithmetic average

cg center of gravity

corr recovery corrected total temperature

d damping

ea elastic axis

eq equivalent standard day quantity

ex compressor exit conditions

h bending

in compressor inlet conditions

ma	mass average
s	structural and mechanical, also isentropic
std	standard day
α	torsion

INTRODUCTION

Successful turbomachinery design requires meeting aero-mechanical as well as aerodynamic performance goals. Flutter and forced response vibrations can exceed blade fatigue strengths and significantly reduce useful blade life. The prediction of flutter and forced response behavior requires knowledge of both the blade structural response and unsteady aerodynamic loading. Structural dynamics analyses [1] used to predict turbomachinery blading structural response provide useful frequency and mode shape predictions as well as the static stress levels. Current first principles unsteady aerodynamic analysis [2] allow the prediction of certain flutter modes. However; at present the amplitude of the forced response can not be predicted using unsteady aerodynamic analysis alone.

Typically forced response vibrations are predicted with a Campbell diagram which identifies the intersections of blade natural frequencies and engine order excitations. Figure I shows the Campbell diagram for the third-stage compressor rotor blade examined herein. Shown on the diagram are the first bending, first torsion, and second bending modes of the compressor blade vibration for the range of compressor operating speeds. The diagram identifies the speed at which each blade mode coincides with engine order excitations, but does not give information about vibration levels. As can be seen in the Campbell diagram it is not usually

possible to avoid all resonances in the operating range of a turbomachine. With multiple blade rows this situation is worse. The blade designer must avoid severe resonances using mostly past experience and extensive testing of flight hardware.

At the resonances identified on the Campbell diagram, forced vibration amplitudes depend only upon the excitation and damping levels [3]. Many sources of excitation exist in multiple blade row turbomachines. Inlet distortion, wakes from upstream blade rows, potential interactions with downstream blade rows, surge, rotating stall, blade tip rubs and shaft unbalance are all potential sources of blade excitation. With appropriate aerodynamic and mechanical design, the effects of surge, rotating stall and blade tip rubs can be eliminated during normal turbomachine operation while the effects of shaft unbalance can be minimized. Some inlet distortion, wakes, and potential interactions will always exist during normal operation.

Turbomachinery blades typically have very little structural, mechanical, and other forms of nonaerodynamic damping [4]. The motion of a vibrating airfoil in a moving air stream is accompanied by an unsteady lift and moment that can either damp or amplify the airfoil vibration depending upon the aerodynamic conditions. The effect of this motion dependent unsteady aerodynamic loading on the blade vibration is referred to as the aerodynamic damping [5],[6]. Since aerodynamic damping can be greater than all other forms of

damping in turbomachinery blades its quantification is very important.

The unsteady aerodynamic theory associated with turbomachinery blade vibration has been developed primarily to circumvent flutter. Reference [7] provides an outline of the development of unsteady aerodynamic theory and outlines the theory. In linearized unsteady aerodynamic theory, forced response is obtained from separate estimates of damping and exciting forces. The exciting or gust force is the unsteady pressure load due to passage of a gust past a rigid airfoil. The aerodynamic damping results from the motion of the airfoil in response to the unsteady gust force. The linearized unsteady aerodynamic theories used to predict flutter may also be used to predict the aerodynamic damping in the forced response problem. With the quantification of the unsteady forces and moments exciting the blade vibrations, the forced response problem can be solved for linear theory.

A survey of measurements and measurement techniques in flutter and forced response research is also presented in [7]. The important tradeoffs between experiments in cascades and low speed rotating rigs that yield detailed data for model verification and experiments in high speed rotating rigs with realistic environments is noted. Despite the difficulty of obtaining detailed data in the high speed rotating rigs it is necessary to evaluate the unsteady aerodynamic models in realistic high speed environments.

Measurement of the aerodynamic damping in a high speed turbomachine appears in the literature. The aerodynamic damping in a high speed rotating fan was measured by Crawley [8]. A flow disturbance was created upstream of the fan. When the disturbance was suddenly removed a modal analysis of the fan response yielded the aerodynamic damping.

In the present investigation the rotor blade aerodynamic damping is determined in a three-stage transonic axial flow compressor. The damping is determined with conventional strain gages. At 70, 80, 90, and 100 percent design corrected speed the total damping associated with the first bending and first torsion modes is determined from rotor blade strain gage broadband power spectra by a single degree of freedom (SDOF) transfer function fit to each mode of interest. By repeating the measurements at three inlet total pressures and assuming that only the aerodynamic damping varies with inlet pressure the aerodynamic damping is determined.

A simplified aero-mechanical blade model is presented to define the aerodynamic damping. The experimental apparatus and data reduction procedures are then presented followed by the experimental results and discussion. The overall aerodynamic performance characteristics for the three-stage transonic axial-flow compressor as well as the experimental Campbell diagrams and aerodynamic damping for the third stage rotor blades are presented and discussed.

AEROMECHANICAL BLADE MODEL

The motion of a vibrating airfoil can be modeled by considering the forces acting on a two-dimensional flat plate or typical section [5],[9],[10]. Figure 2 depicts a two-dimensional flat plate airfoil of unit width immersed in a uniform flow. The oncoming flow approaches the airfoil with the speed U. The airfoil is constrained to two degrees of freedom: bending h, positive downward measured at the elastic axis; and torsion, α, positive nose up about the elastic axis. For the general case considered the elastic axis and the center of gravity of the airfoil section do not coincide. The elastic axis is shown rearward of the center of gravity in figure 2.

The forces acting on the airfoil are: the unsteady lift L; the excitation P; the spring force $k_h h$; and the damping force $c_h h$. The unsteady lift, L, is the lift due to the oscillating motion of the airfoil in the uniform oncoming flow. The excitation, P, can be aerodynamic or mechanical. Aerodynamic excitations result from disturbances in the flow. For linearized unsteady aerodynamic theory the effect of these disturbances in the flow is equivalent to the excitation, P, and a uniform flow. The damping force is expressed in terms of a viscous damping coefficient [3]. The damping force accounts for the structural and mechanical contributions to the total damping. The structural damping is due to material hysteresis. The mechanical damping is due to friction between moving parts. Neither the structural,

mechanical, or the aerodynamic damping which is due to the unsteady lift L are the result of viscous forces. The viscous damping identifies that the mechanical and structural damping is assumed to be proportional to the vibration velocity as is the case for a viscous damper.

Newton's second law is

$$\sum \bar{F} = m\ddot{\bar{r}}_{cg}$$

where $\ddot{\bar{r}}_{cg}$ is the acceleration of the center of gravity. The displacement of the center of gravity is shown in figure 2.

$$\bar{r}_{cg} = (h - a \sin \alpha)\bar{i}_2$$

Differentiating twice gives

$$\dot{\bar{r}}_{cg} = (\dot{h} - a \dot{\alpha} \cos \alpha)\bar{i}_2$$

and

$$\ddot{\bar{r}}_{cg} = (\ddot{h} + a(\dot{\alpha})^2 \sin \alpha - a \ddot{\alpha} \cos \alpha)\bar{i}_2$$

Noting all forces act in the $\bar{i}_2$ direction gives

$$-L + P - c_h\dot{h} - k_h h = m (\ddot{h} - a \ddot{\alpha} \cos \alpha + a (\dot{\alpha})^2 \sin \alpha)$$

Noting for small motion $\cos \alpha \sim 1$ and $\sin \alpha \sim 0$ we have

$$m\ddot{h} - ma\ddot{\alpha} + c_h\dot{h} + k_h h = -L + P \qquad (1)$$

The moments acting on the airfoil section are: the unsteady aerodynamic moment M; the exciting moment Q; the moment due to the torsional stiffness $k_\alpha\alpha$; and the damping moment $c_\alpha\dot{\alpha}$. The unsteady aerodynamic moment, M, is due to the motion of the airfoil in the uniform flow. The exciting moment, Q, like the

exciting force, P, can be aerodynamic or mechanical. The moments are summed about the elastic axis with

$$\sum M_{ea} = I_{cg}\ddot{\alpha} + \bar{r}_a \times m\ddot{\bar{r}}_{cg}$$

The cross product is evaluated with

$$\bar{r}_a = -a \cos \alpha \, i_1 - a \sin \alpha \, i_2$$

where the unit vectors are shown in figure 2. The cross product becomes

$$\bar{r}_a \times m\ddot{\bar{r}}_{cg} = -am \cos \alpha \, (\ddot{h} - a \ddot{\alpha} \cos \alpha + a \dot{\alpha}^2 \sin \alpha)$$

for small motion

$$\bar{r}_a \times m\ddot{\bar{r}}_{cg} = -ma\ddot{h} + ma^2\ddot{\alpha}$$

Summing moments gives

$$M + Q - c_\alpha \dot{\alpha} - k_\alpha \alpha = I_{cg}\ddot{\alpha} + ma^2\ddot{\alpha} - ma\ddot{h}$$

noting

$$I_{ea} = I_{cg} + ma^2$$

gives after rearranging

$$-ma\ddot{h} + I_{ea}\ddot{\alpha} + c_\alpha \dot{\alpha} + k_\alpha \alpha = M + Q \qquad (2)$$

Equations (1) and (2) describe the coupled bending torsion motion of a two-dimensional flat plate airfoil. The inertia terms couple the torsion and bending modes when the center of gravity and elastic axis are not coincident. Any torsional oscillation will be accompanied by bending oscillations and any bending motion must be accompanied by torsional motion. For strongly coupled modes the unsteady aerodynamics due to bending can not be ignored for

torsional vibration and that due to torsion can not be ignored for bending modes.

In order to define aerodynamic damping it is useful to consider uncoupled modes. This greatly reduces the number of unsteady aerodynamic terms without sacrificing physical significance.

The motion of a flat plate airfoil constrained to bending vibration is governed by

$$m\ddot{h} + c_h\dot{h} + k_h h = -L + P \tag{3}$$

Introducing the undamped natural frequency

$$\omega_h = \sqrt{\frac{k_h}{m}}$$

and dimensionless time

$$\tau = \frac{Ut}{b}$$

equation (3) becomes

$$m\frac{U^2}{b^2}h'' + c_h\frac{U}{b}h' + \omega_h mh = -L + P \tag{4}$$

The unsteady lift force is given [9] as

$$L = 2\pi\rho U^2 \int_{-\infty}^{\infty} \Phi(\tau - \tau_o)h''(\tau_o)d\tau_o + \rho\pi U^2 h'' \tag{5}$$

Here Φ is Wagner's function which is the result of the unsteady circulation induced by the motion of the airfoil. The second term in equation (5) is an apparent mass force. Together equations (4) and (5) define the single degree of freedom bending motion of a flat plate airfoil.

In the case of a periodic excitation, the integral in equation (5) may be evaluated. With

$$P = P_o e^{ik\tau}, \qquad h = h_o e^{ik\tau}$$

and the reduced frequency

$$k = \frac{\omega b}{U}$$

equations (4) and (5) become

$$m\frac{U^2}{b^2}(-k^2)h_o + c_h\frac{U}{b}(ik)h_o + \omega_h{}^2 m h_o = -2\pi\rho U^2(ikC(k))h_o - \rho\pi U^2(-k^2)h_o + P_o \qquad (6)$$

Here $C(k)$ is Theodorsen's function [9] which may be written as

$$C(k) = F(k) + iG(k)$$

Substituting this into equation (6) gives

$$\frac{h_o}{P_o} = \frac{1}{-\left(\pi\rho b^2 + m + 2\pi\rho b^2\frac{G(k)}{k}\right)\omega^2 + i\omega(c_h + 2\pi\rho UbF(k)) + m\omega_h{}^2} \qquad (7)$$

The terms in equation (7) can be identified by comparison with the response of the airfoil in the absence of the unsteady aerodynamic terms which is

$$\frac{h_o}{P_o} = \frac{1}{-m\omega^2 + i\omega c_h + m\omega_h{}^2} \qquad (8)$$

Comparing equations (7) and (8) the terms in equation (7) can be identified as

$$\text{mass} = \pi\rho b^2 + m + 2\pi\rho b^2\frac{G(k)}{k} \qquad (9)$$

$$\text{damping} = c_h + 2\pi\rho UbF(k) \tag{10}$$

$$\text{stiffness} = m\omega_h^2 \tag{11}$$

The effect of the unsteady aerodynamic loading on blade motion will be shown by comparing the magnitude of each term in each of equations (9), (10), and (11). Each term will be evaluated for the third-stage rotor blade investigated herein. Turbomachinery aeroelastic analysis are commonly performed on a typical section taken near 75 percent span from the rotor hub [7]. The following parameters taken from the compressor aerodynamic design are at the streamline 78.5 percent span from the rotor hub and correspond to standard day conditions.

density, $\rho = 0.1341$ lbm/ft^3

relative velocity, $U = 1416$ ft/sec

semichord, $b = 0.07653$ ft

The following data correspond to the entire third-stage rotor blade. The blade natural frequency in the first bending mode at the design speed is taken from figure 1.

natural frequency, $\omega_h = 9050$ rad/sec

blade span, $l = 0.1885$ ft

blade mass, $m_b = 0.0543$ lbm

Equation (9) for the mass of the airfoil immersed in the airstream may be rewritten as

$$\pi\rho b^2 + m + 2\pi\rho b^2 \frac{G(k)}{k} = \pi\rho b^2\left(1 + \mu - \frac{2G(k)}{k}\right) \tag{12}$$

where

$$\mu = \frac{m}{\pi\rho b^2}$$

is called the mass ratio and is roughly the ratio of the mass of the airfoil to the mass of air it displaces. For the third-stage rotor blades $\mu = .94$ at the design condition hence the blade mass is 94 times the mass of air it displaces at standard day condition. For all operating points tested herein the inlet pressure is less than the standard day pressure, the density is less than the standard day density and the mass ratio is greater than the design value. At part speed the pressure ratio is also less than the design value and the mass ratio even greater.

The term in equation (12) due to the unsteady circulation, $2G(k)/k$, is tabulated as a function of the reduced frequency in table 6.1 of [9]. For the first bending mode at design speed the reduced frequency is $k = 0.49$ and $2G(k)/k = -0.62$ and does not alter the effective blade mass. For typical turbomachinery applications the mass of the blade is sufficiently large in comparison to the air that it displaces that the unsteady aerodynamic loading does not alter the effective mass of the blade.

The aerodynamic portion of the damping in equation (10) is

$$c_a = 2\pi\rho UbF(k) \qquad (13)$$

Evaluating this at the design condition for the first bending mode of the third stage rotor blade and again referring to table 6.1 in [9] gives $c_a = 54.8$ lbm*rad/sec/ft. The nonaerodynamic damping in equation (10) will be evaluated from the experimental results

presented herein. At the design corrected speed the experimental nonaerodynamic damping ratio in the first bending mode is $\zeta_s = 0.00134$ (see figure 15). The damping coefficient is related to the damping ratio as

$$c_h = 2m\omega_h\zeta \tag{14}$$

Since the measured damping ratio and predicted natural frequency are modal quantities, the mass that appears in equation (14) is the modal mass which is 1/4 the total beam mass for a uniform cantilever beam [11]. The nonaerodynamic damping for the third stage rotor blade is $c_h = 0.329$ lbm*rad/sec. This value corresponds to the entire span where as the aerodynamic damping determined from equation (13) corresponds to a unit span. Assuming the aerodynamic damping is constant across the span of the rotor blade the total aerodynamic damping for the blade is $c_a = 10.3$ lbm*rad/sec. It is seen that the aerodynamic damping, $c_a = 10.3$ lbm*rad/sec, is much greater than the nonaerodynamic damping, $c_h = 0.329$ lbm*rad/sec.

The unsteady aerodynamics of an isolated flat plate airfoil in an incompressible flow does not adequately describe the flow in a high speed turbomachine. The effects of cascaded blades as well as compressibility are important factors in determining the unsteady aerodynamic loading. However, the simple model outlined above does highlight features typically seen in turbomachinery applications. The major portion of the damping in turbomachinery blades can be attributed to the unsteady aerodynamic loading while the mass and

stiffness of the blades are not significantly affected by the unsteady aerodynamic loading.

In different applications the blade mass and stiffness could be affected by the unsteady aerodynamic loading. Hollow or composite blades, compressors operating with high inlet pressures due to high speed flight, and the rear stages of very high pressure ratio compressors are each possible applications.

The interested reader is referred to [5],[9],[10] for more details of the aeroelastic results presented above. The unsteady aerodynamics suitable for turbomachinery flows are presented in [7].

APPARATUS AND PROCEDURE

Research Compressor

A three-stage transonic axial-flow compressor was experimentally studied in the NASA Lewis Research Center Multistage Compressor Test Facility. The compressor is the first three stages of a five stage core compressor design, designated 74B. The low aspect ratio compressor is typical of the front stages of an advanced aircraft engine core compressor. The design point aerodynamic performance goals for the first three stages are 65.5 lbm/sec mass flow and 4.5:1 total pressure ratio. The first-stage rotor blade is designed for a 1.4 inlet relative Mach number at the leading edge tip with no inlet swirl. The flow is turned to the axial direction out of each stator of the high reaction design. Blade design loss values were estimated high to favor off design performance and stage matching. This resulted in a low design efficiency of 80 percent. The uncambered inlet guide vane (IGV) has a fixed leading edge and resettable trailing edge. The IGV trailing edge and three stator blade rows are equipped with remotely controllable variable geometry. The aerodynamic design of compressor 74B parallels that of compressor 74A which is discussed in [12].

The third-stage rotor blade is sketched in figure 3. The compressor blade base slides into a slot machined into the rotor wheel. The predicted frequency response for the blade was shown in

figure 1. Aerodynamic and aeroelastic parameters for the blade are listed on page 10.

Compressor Test Facility

The NASA Lewis Multistage Compressor Test Facility is described in detail in [13]. A schematic diagram of the facility is shown in figure 4. Briefly, atmospheric air enters the test facility through a filtered inlet located on the roof of the building and flows through a flow measuring orifice, and then through two inlet butterfly throttle valves which control the pressure in the inlet plenum tank. The air then passes through the test compressor and into the collector to be dumped to either the atmosphere or to an altitude exhaust system. The altitude exhaust system allows running the compressor at low inlet pressures without the need for the compressor to overcome the piping losses. Mass flow is controlled with a sleeve valve downstream of the compressor. This valve is located approximately one compressor length downstream of the third-stage stator trailing edge. With the altitude exhaust system operating the valve remains choked during compressor operation. The present series of experiments were conducted with the altitude exhaust system operating. The compressor is driven with a 15 000 hp synchronous electric motor through a 5.21:1 speed increasing gearbox. The motor speed is varied with variable frequency power generated in the basement of the building.

Instrumentation

Two iron-constantan thermocouples are located in the compressor inlet plenum for sensing inlet total temperature. All research thermocouples are connected to one of three HY-CAL model 401 reference blocks located in the test cell. Each reference block temperature is read with a platinum resistance temperature sensor. The compressor inlet total pressure is assumed equal to plenum static pressure which is measured by four wall static taps located approximately 90° apart in the plenum tank. Two manifolds each connect two static taps. The pressure is taken to be the average of the pressure measured in each manifold with a calibrated 15 psid Bell and Howell model 4-451 pressure transducer.

The compressor exit conditions are measured with four rakes located approximately 90° apart 2.5 in. downstream of the third-stage stator trailing edge. The rake measurement plane is shown on compressor meridional view in figure 5. Each rake has five total-pressure and five total-temperature elements at 10, 30, 50, 70, and 90 percent of the annulus span. The rake thermocouples are Chromel-constantan. Static pressures at each rake element are linearly interpolated from the inner and outer wall static-pressure measurements in the constant inner and outer diameter region of the annulus. At the design equivalent speed at the maximum efficiency stator schedule, performance was measured with two of four rakes in place.

Pressures at the compressor exit are measured with two Scanivalve model SBC80 pressure scanning systems. The high reference pressures for the pressure scanning systems are provided by Mansfield Green model mk-100 dead weight testers. The low reference pressures are open to the test cell atmosphere. During testing with the full lineup of steady state instrumentation 50 psid pressure transducers were used with 40 psig reference pressures. The aerodynamic data at design equivalent speed with the stators reset were obtained with 25 psid pressure transducers and 25 psig reference pressures.

The compressor mass flow is determined with a standard ASME sharp-edge thin-plate orifice with 1-D and 1/2-D taps. The 19 in. ID orifice plate is centered in a 48 in. OD by 1/4 in. wall pipe. Four static pressure taps approximately 90° apart are located 1 pipe diameter upstream and 1/2 pipe diameter downstream of the orifice plate. At each location two manifolds connect two taps. The pressures in each upstream manifold are measured with calibrated 1 psid Bell and Howell model 4-451 pressure transducers. The pressure difference between each upstream manifold and a corresponding downstream manifold are measured with 2 psid Bell and Howell model 4-451 pressure transducers. The orifice temperature is measured with two iron constantan thermocouples immersed in the flow 2 pipe diameters downstream of the orifice. A Computer Measurements Corporation model 614A electronic speed counter with a

Electro model 3010 HT-4-957 magnetic pickup located above a 96-tooth gear on the drive motor shaft measure the compressor speed (rpm).

Steady state aerodynamic performance data were recorded and monitored during the test with a lab wide data system called ESCORT. The version used in the present series of experiments is ESCORT II. The analog data is digitized in the test cell control room with a Neff model 620 digitizer and along with the digital scanivalve output transported over telephone lines to a dedicated PDP 11-34 minicomputer located in a central computing facility. The minicomputer provides online test monitoring and storage of selected data points for subsequent retrieval. Post processing was performed on an IBM 370/3033 computer.

Four blades of each of the three rotor and stator blade rows are instrumented with two Micro-Measurments model WD-DY-062AP-350 350 Ohm strain gages. The gages with approximately 0.0625 in. square active elements are located at or near the predicted position of maximum strain in the first bending and first torsion modes of the airfoils. Rotor blade strain gage signals are obtained from the rotating environment with a rotating data package described in [14]. Power is delivered to the rotating data package and data is obtained from it with a rotating transformer. A switching circuit provides the output from a single gage at any time. The strain gage signals can be accessed in a sequential scanning pattern or a single gage can be monitored. The stator blade strain gage signals are connected to the control room with a Cunningham

model 000 451 001 scanner with one channel accessible at a given time. Stator strain gage signals can also be scanned sequentially or monitored individually.

The output from a Bently Nevada model S109 proximity probe located to measure the orbit of the shaft connecting the compressor and gearbox provides the compressor one per rev frequency for signal analysis. Rotor and stator strain gage signals and the 1/rev signal are recorded on a Sabre VII FM tape recorder for post processing. The data are processed with a GenRad model 2502 signal analysis system.

The estimated errors of the data based upon inherent inaccuracies of the instrumentation and recording system are as follows:

Mass flow, lbm/sec	$\pm$0.7
Temperature, °R	$\pm$1
Inlet total pressure, psi	$\pm$0.2
Outlet total pressure, psi	$\pm$0.6
Outlet static pressure, psi	$\pm$0.6
Rotative speed, rpm	$\pm$30
Rotor blade strain, percent	$\pm$5

The aerodynamic measurements errors are taken from [12] for a similar test. The strain error is taken from [14].

Test Procedure

The compressor overall aerodynamic performance is obtained by operating the compressor at constant equivalent speed and decreasing the mass flow with the downstream throttle. Data are recorded at successive throttle positions from the maximum flow to stalled flow. Stalled flow is identified by increases in stress

levels, exit temperature and decreases in pressure ratio, weight flow, and efficiency.

The procedure used to establish the IGV-stator setting angles for maximum overall efficiency at each speed is as follows. The compressor is operated from choke to stall at each speed to determine the maximum efficiency throttle position with the design setting angles. The compressor is then operated at the maximum efficiency throttle position while resetting the IGV's and stators. First the IGV's are reset searching for the maximum efficiency setting angle. Next with the IGV's in their maximum efficiency position the first stage stator vanes are reset searching for the maximum efficiency. Then with the IGV's and stator one in their maximum efficiency positions the second stage stator is reset searching for the maximum efficiency position. The procedure is them repeated for the third stage stator with the upstream blade rows at their maximum efficiency positions. Following resetting the third stage stator, the inlet guide vane is reset again searching for the maximum efficiency. This completes the procedure, no attempt is made to reset any of the downstream stators again. The compressor performance is then obtained with the maximum efficiency reset schedule from choke to stall.

Rotor blade strain gage data are obtained by recording the strain gage data at successive throttle positions along a constant equivalent speed line as for the overall aerodynamic performance data. Strain gage data for Campbell diagrams is recorded with the

rotating data system scanning at 1.6 sec/gage. The data recorded to identify the damping is recorded for 6 min with the data system fixed on one gage. This is repeated for each gage. When obtaining strain gage data the aerodynamic performance is also obtained.

Overall Performance Data Reduction

The compressor overall aerodynamic performance is presented as the total pressure ratio and adiabatic efficiency as a function of equivalent mass flow for different equivalent speeds [15],[16]. The equivalent speed is defined as

$$N_{eq} = \frac{N}{\sqrt{\theta}} \tag{15}$$

where θ is the ratio of measured inlet plenum total temperature to the standard temperature of 518.7 °R. The equivalent mass flow is

$$\dot{m}_{eq} = \frac{\dot{m}\sqrt{\theta}}{\delta} \tag{16}$$

where δ is the ratio of inlet plenum total pressure to the standard pressure of 14.7 psia. The mass flow is [17]

$$\dot{m} = 189.34\left(1 - 0.299\,\frac{\Delta p}{p}\right)\sqrt{\frac{p\Delta p}{t}} \tag{17}$$

The total pressure ratio is determined from the mass averaged total pressure at the exit rake measuring station and the inlet plenum pressure. The mass averaged exit total pressure is

$$\bar{P}_{ex,ma} = \frac{\sum P\dot{dm}}{\sum \dot{dm}} \tag{18}$$

Each term in equation (18) is evaluated at the exit rake station and the sums are taken over the five elements of the four rakes.

The increment of flow assigned to each rake element is

$$d\dot{m} = \sqrt{\frac{\gamma g}{R}} \frac{P}{\sqrt{T_{corr}}} M \left(1 + \frac{\gamma - 1}{2} M^2\right)^{-\frac{\gamma+1}{2(\gamma-1)}} dA \qquad (19)$$

Each term in equation (19) is obtained as follows. The element of area, dA, assigned to each measurement is 25 percent of the area between the streamlines midway between the particular measurement and the measurement above and below. For measurements adjacent to the case and the hub an area corresponding to the design blockage at the compressor exit of 5.1 percent of the total annulus area is subtracted.

The specific heat ratio at the exit is determined as follows: An average static to total pressure ratio at the rake station is determined as

$$\left(\frac{\bar{p}}{P}\right)_a = \frac{1}{n} \sum \frac{p}{P}$$

for the n total pressure measurements. The static pressure is taken to be that at the outer wall measured circumferentially nearest the apprcpriate rake. With the arithmetic average of the exit total temperatures given by

$$\bar{T}_a = \frac{1}{n} \Sigma T$$

the static temperature is

$$\bar{t}_a = \bar{T}_a \left(\frac{\bar{p}}{P}\right)_a^{0.2857}$$

The specific heat is determined from

$$C_p = 0.23747 + 0.21962e\text{-}04*\bar{t}_a - 0.87792e\text{-}07*\bar{t}_a^2 + 0.13991e\text{-}09*\bar{t}_a^3$$

$$- 0.78056e\text{-}13 * \bar{t}_a^4 + 0.15043e\text{-}16 * \bar{t}_a^5$$

and the specific heat ratio from

$$\gamma = \frac{1}{1 - \frac{R}{JC_p}}$$

The Mach numbers are determined from

$$M = \left\{ \frac{2}{\gamma - 1} \left[\left(\frac{p}{P} \right)^{-\frac{\gamma-1}{\gamma}} - 1 \right] \right\}^{1/2}$$

where the static pressure at each rake radial position is linearly interpolated from measured values at the inner and outer walls. The total temperatures used in equation (19) are corrected for recovery variation with Mach number [18] with

$$T_{corr} = \frac{T}{1 - \Delta}$$

The recovery-correction factor, Δ , is determined from calibration of each of the rakes in a calibration jet. The value of the recovery correction is small for the shielded thermocouples and the closeness of the calibration data warranted using a single correction curve. The curve is given in figure 6.

The adiabatic efficiency is

$$\eta_{ad} = \frac{H_{ex,s} - H_{in}}{H_{ex} - H_{in}} \qquad (20)$$

where H is the stagnation enthalpy of the flow. For constant specific heats this may be written

$$\eta_{ad} = \frac{(P_{ex}/P_{in})^{\frac{\gamma-1}{\gamma}} - 1}{T_{ex}/T_{in} - 1} \tag{21}$$

The adiabatic efficiency is averaged as follows. The numerator is mass averaged and defines the mass averaged isentropic temperature rise ratio

$$\frac{\overline{\Delta T}_{s,ma}}{T_{in}} = \frac{\sum\left[(P_{ex}/P_{in})^{\frac{\gamma-1}{\gamma}} - 1\right]\dot{dm}}{\sum\dot{dm}} \tag{22}$$

This may be used directly in equation (21). The mass averaged total temperature ratio is evaluated as

$$\frac{T_{ex,ma}}{T_{in}} = \frac{1}{T_{in}} \frac{\sum T_{ex,corr}\,\dot{dm}}{\sum\dot{dm}} \tag{23}$$

The mass averages calculated in equations (22) and (23) are performed as is done for equation (18).

Rotor Blade Strain Gage Data Reduction

The rotor blade dynamic stress is related to the measured dynamic strain with Hooke's law

$$\sigma = \varepsilon E$$

where σ is the stress, ε the measured strain, and E Young's modulus for the Ti-6Al-4V blades. The measured strain is given by

$$\varepsilon = \frac{\Delta R}{RG}$$

where R is the strain gage resistance and G the gage factor which is supplied with the strain gages. The voltage output of the data system is related to the resistance change as

$$V = I\,A(f)\,\Delta R$$

where I is the 5 mA constant current and A(f) is the system gain which is a function of frequency. The stress is then given by

$$\sigma = \frac{E}{IRG\ A(f)}\ V \tag{24}$$

The rotating data system gain is determined prior to testing. A 350 Ohm resistor is used to simulate the 350 Ohm strain gage. An Interstate model F74 Oscillator provides the variable voltage across the resistor. A 1.94 mV excitation was selected to provide a 1 V peak to peak output at the strain gage readout. The input and output voltage levels were each read with B and K model 2427 VTVM's. The rotating data system gain is shown in figure 7. The attenuation of the gain above 3000 Hz is due to a 5000 Hz filter used to separate the data from the 20 kHz power supplied to the rotating data system. An average gain is obtained by averaging the gain at the predicted first bending frequencies for each of the three rotors. The predicted first bending frequencies at the design speed are 590, 998, and 1440 Hz. The average gain is 178.0. With the average gain the stress is related to the output voltage by

$$\sigma = 16\ 570\ V \tag{25}$$

The average gain results in an under predicted stress of 8 percent at 400 Hz and an over predicted stress of 7 percent at 2000 Hz. Above 3000 Hz the stress is again under predicted. The errors involved in determining the damping in the third-stage rotor first bending mode are small and neglected. In the case of the

third-stage rotor first torsion mode the variable gain results in only small differences in the measured damping.

Campbell diagrams are constructed by plotting the rotor blade response frequency against the compressor rpm. The blade response frequency is taken from the peaks in the strain gage output power spectra. The compressor rpm is obtained from peaks in the power spectra of the one per rev signal. The data is filtered at 5000 Hz and digitized at 12 800 samples/sec to avoid aliasing. The power spectra [19] are determined from a single squared Fast Fourier Transform (FFT) of 8192 data samples and have a frequency resolution of 1.56 Hz. During initial testing a twice per revolution with high harmonic content was recorded instead of the once per revolution. In this case the rpm was determined from the higher harmonics resulting in a greater resolution in determining the mechanical speed.

Alternating stress levels in each mode are determined from the peak positive and negative stresses in a 512 sample time trace which is digitized at 12 800 samples/sec and filtered at 5000 Hz to avoid aliasing. The alternating stress is taken as the difference between the two peak stresses. This does not necessarily correspond to the stress in each mode since more than one mode may be contributing; however, for the resonant stresses measured the response was primarily in a single mode.

The damping in each mode is determined by curve fitting a SDOF transfer function to the nonsynchronous portion of the strain gage

power spectra in the vicinity of each mode. The data are filtered at 5000 Hz and digitized at 12 800 samples/sec . A Hanning window with compensation for lost energy is applied to reduce truncation errors. The raw power spectra is computed from the squared FFT of 8192 data samples. The power spectra is determined from nominally 300 averaged raw power spectra.

Estimates of the statistical properties of power spectrum estimates are given in [20]. The normalized bias error associated with the power spectrum is to a first approximation

$$e_b \sim \frac{B_e^2 G_{xx}''}{24\, G_{xx}} \tag{26}$$

where B_e is the frequency resolution or spacing in the FFT used to calculate the power spectrum. For a SDOF system with white noise input at resonance

$$e_b \sim -\frac{1}{3}\left(\frac{B_e}{B_r}\right)^2$$

where B_r is the 1/2 power point bandwidth of the SDOF system. For small damping ratios, $\zeta << 1$ the 1/2 power bandwidth is

$$B_r \sim 2\, f_n\, \zeta$$

The greatest bias errors in the measurements of the third stage rotor blades occurs in tne first bending mode at the lowest inlet pressures. With $\zeta = 0.005$, $f_n = 1300$ and $B_e = 1.5625$; $e_b = 0.004$. The normalized variance or random error is given by

$$e_r = \frac{1}{\sqrt{n}} \tag{27}$$

For nominally 300 averages this is $e_r = 0.06$. The errors in the power spectrum estimation do not limit the identification of the rotor blade damping.

The data is digitized and the power spectrum is computed and written to disk. The averaged power spectra is read from disk and a least squares fit is performed to each mode to determine the natural frequency and damping ratio. The least squares procedure is developed below.

The frequency response function [3],[19],[20] is defined as

$$H(f) = \frac{Y(f)}{X(f)} \tag{28}$$

where $X(f)$ and $Y(f)$ are the Fourier transforms of the input and output respectively. Squaring this gives

$$|H(f)|^2 = \frac{G_{yy}(f)}{G_{xx}(f)} \tag{29}$$

where $G_{xx}(f)$ and $G_{yy}(f)$ are the input and output power spectrum, respectively. Assuming the input spectrum is Gaussian or white noise the input power spectrum is constant. Writing the frequency response function for a SDOF system with equivalent viscous damping gives

$$\frac{G_{yy}(f)}{G_{xx}} = \frac{1/k^2}{\left[1 - (f/f_n)^2\right]^2 + \left[2\zeta(f/f_n)\right]^2} \tag{30}$$

The natural frequency, damping ratio and the constant k^2/G_{xx} are determined from a least square fit to equation (30) for each mode of interest. It should be noted to simplify the notation the

spring constant, k, is expressed as force per unit stress. The transfer function then represents the stress per unit force as a function of frequency.

The least squares procedure is developed as follows: Rewrite equation (30) as

$$\left[1 - (f/f_n)^2\right]^2 + \left[2\zeta(f/f_n)\right]^2 = \frac{G_{xx}}{k^2 G_{yy}(f)}$$

expanding the squared terms in brackets gives

$$(f/f_n)^4 - 2(f/f_n)^2 + 1 + 4\zeta^2(f/f_n)^2 = \frac{G_{xx}}{k^2 G_{yy}(f)}$$

multiplying through by k^2/G_{xx} gives

$$\frac{k^2}{G_{xx} f_n^4} f^4 - (2 - 4\zeta^2) \frac{k^2}{G_{xx} f_n^2} f^2 + \frac{k^2}{G_{xx}} = \frac{1}{G_{yy}(f)}$$

This can be written as

$$c_1 + c_2 x + c_3 x^2 = y \qquad (31)$$

where

$$c_1 = \frac{k^2}{G_{xx}}, \qquad c_2 = -(2 - 4\zeta^2) \frac{k^2}{G_{xx} f_n^2}, \qquad c_3 = \frac{k^2}{G_{xx} f_n^4}$$

$$x = f^2, \qquad y = \frac{1}{G_{yy}(f)}. \qquad (31)$$

The least squares procedure [21] is applied to equation (31) by minimizing the square error associated with n data points with respect to the coefficients c_1, c_2, and c_3. The error r for each data point is

$$r_i = c_1 + c_2 x_i + c_3 x_i^2 - y_i \tag{32}$$

Minimizing the square error requires

$$\frac{\partial}{\partial c_k} \sum_{i=1}^{n} (r_i)^2 = 0 \qquad k = 1,2,3 \tag{33}$$

which is

$$\sum_{i=1}^{n} r_i \frac{\partial r_i}{\partial c_k} = 0 \qquad k = 1,2,3$$

Writing out the three resulting equations give

$$\begin{aligned} nc_1 + (\Sigma x_i)c_2 + (\Sigma x_i^2)c_3 - \Sigma y_i &= 0 \\ (\Sigma x_i)c_1 + (\Sigma x_i^2)c_2 + (\Sigma x_i^3)c_3 - \Sigma x_i y_i &= 0 \\ (\Sigma x_i^2)c_1 + (\Sigma x_i^3)c_2 + (\Sigma x_i^4)c_3 - \Sigma x_i y_i &= 0 \end{aligned} \tag{34}$$

Equations (34) are solved for the three coefficients.

The aerodynamic damping is determined from combined damping measurements at three inlet total pressures. The aerodynamic damping force is due to the unsteady aerodynamic lift and moment generated by tne motion of the vibrating blades and may be scaled by the dynamic pressure of the flow. The aerodynamic damping force due to translation of the blade may be written as

$$F_{da} = F_{da,std}(q/q_{std})$$

where std refers to standard day and

$$q = 1/2\ \rho U^2 = 1/2\ \gamma p M^2$$

is the dynamic pressure. Excluding small Reynolds number effects, the Mach numbers in the compressor are a function only of the equivalent speed, equivalent mass flow, and pressure ratio. Since

the specific heat ratio is also essentially constant for the range of conditions seen in the experiments, the aerodynamic damping force scales with the static pressure. The static pressure at any point in the compressor depends only on the inlet total pressure for a given equivalent speed, equivalent mass flow and pressure ratio. The aerodynamic damping force may then be scaled with the inlet total pressure for a given equivalent speed, equivalent mass flow, and pressure ratio.

$$F_{da} = F_{da,std}\left(\frac{P_{in}}{P_{std}}\right) \tag{35}$$

The combined damping force may be written as

$$F_d = F_{ds} + F_{da,std}\left(\frac{P_{in}}{P_{std}}\right) \tag{36}$$

For a SDOF with viscous damping undergoing periodic motion the damping force may be written as

$$F_d = i\omega c x_o (e^{i\omega t})$$

and the damping ratio

$$\zeta = \frac{c}{2\omega_n m}$$

can be written as

$$\zeta = \frac{Fd}{i\omega x_o (2\omega_n m) e^{i\omega t}}$$

Dividing equation (36) by the denominator above gives

$$\zeta = \zeta_s + \zeta_{a,std}\left(\frac{P_{in}}{P_{std}}\right) \tag{37}$$

Assuming the structural and mechanical damping ratio does not change with inlet pressure the structural and mechanical damping and the aerodynamic damping are determined from (37).

The assumption of constant nonaerodynamic damping is supported as follows. The majority of the nonaerodynamic damping in bending modes is expected to be friction at the blade root. The friction at the blade root depends upon the normal load at the contacting surfaces and the amplitude of the blade motion. The normal load is almost entirely set by centrifugal forces on the rotor blades and should not change with inlet pressure. In addition the amplitude of vibration will not change significantly if the aerodynamic damping is the majority of the damping. This can be shown as follows: The blade response at resonance is given by

$$\sigma = \frac{F/k}{2\zeta}$$

Since the aerodynamic force is proportional to the inlet total pressure and using equation (37) gives

$$\sigma = \frac{(P_{in}/P_{std})F_{std}/k}{2[\zeta_s + \zeta_{a,std}(P_{in}/P_{std})]}$$

If all the damping is aerodynamic the vibration amplitude will not change with inlet pressure. If the vibration amplitude and the normal load do not change with inlet pressure, friction at the blade root will not change with inlet pressure. Since structural damping is anticipated to be very small for both modes, any changes in the structural damping can be ignored.

RESULTS AND DISCUSSION

Overall Aerodynamic Performance

The overall aerodynamic performance of the three-stage transonic axial compressor with the inlet guide vanes and stators at their design setting angles is shown in figure 8. The compressor total pressure ratio and adiabatic efficiency are plotted against equivalent mass flow for 50, 70, 80, 90, and 100 percent design equivalent speed. The overall performance data were acquired at a nominal compressor inlet total pressure of 0.5 atm. The compressor mass flow exceeds the design flow at the design speed. The excess in flow rate is comparable to that of a similar compressor, designated 74A, reported in [12].

The compressor's overall performance with the inlet guide vanes and stators reset for maximum efficiency at each speed is presented in figure 9. Again the overall performance data were acquired with the compressor inlet total pressure nominally 0.5 atm. Table 1 lists the vane reset schedule at each speed and figure 10 defines the vane reset direction. The flow exceeds its design value as it did prior to resetting the vanes. No attempt was made to obtain the design flow while resetting the vanes. The efficiency at the design speed increased nearly 6 points from that with the vanes at their design positions. A low design efficiency had been selected to benefit part speed performance and matching. The increase in efficiency at the design speed is consistent with the performance of compressor 74A in reference [12].

Campbell Diagrams

Campbell diagrams and measured stress levels for the third-stage rotor blade row are presented in figures 11-13. The first bending and first torsion modes measured on the same blade are shown in each diagram. The response in each mode is identified with the gage positioned to measure the maximum response in that mode. The open symbols are the measured response frequencies of the highest stress in each mode at each mechanical speed shown. The solid lines are the blade natural frequencies predicted by finite element analysis. Also shown are the measured stress levels. For convenience, only stresses in the indicated modes above 500 psi are shown. The three figures correspond to the three third stage rotor blades for which the aerodynamic damping is presented. The strain gage numbers are noted on the figures. Data was not obtained and is not shown in the first bending mode below 11710 rpm for gage 24 in figure 13.

The data shown in the Campbell diagrams was acquired with the compressor throttle in its full open position. The data at the full open position are shown so the effects of stall at low speeds does not complicate the data.

The predicted frequency response describes the trends in the first bending mode. The forced response vibrations are excited by unsteady flows at the engine order frequencies. The measured frequencies do not trace out the mode frequency variation with speed since the excitations do not coincide with the natural

frequency at all operating speeds. The highest stresses occur at resonance where the engine order and natural frequencies coincide. High stresses are predicted at 11 710 rpm in figures 11 and 13 and at 14 160 rpm in figure 13. At several other operating points the high stresses are not coincident with the predictions. Considerable variation in response is seen for the different gages. The variation is attributed to manufacturing variations resulting in different natural frequencies of the individual blades.

The greatest stress in the first bending mode occurs at 11 710 rpm at 7/rev as shown in figure 13. The stress level shown is 6000 psi. The compressor has 32 second-stage rotor blades and 39 third- tage rotor blades. The difference in the number of rotor blades causes an unsteady flow for the second-stage stator row due to the wakes convected downstream from the second-stage rotors and the upstream potential influence of the third-stage rotor blades. The third-stage rotor blades moving through the unsteady wake pattern from the second stage stator row experience this 7/rev excitation.

The data in the first torsion mode is not described by the predicted frequency curve. The response frequency decreases with compressor rpm for each of the three blades shown. Since the excitation frequencies are so closely spaced this is attributed to a change in the natural frequency. This decrease may be due to increased flexibility of the rotor wheels with speed or a decrease in stiffness of the blades due to temperature. The rotor-blade

finite-element analysis was performed using design speed temperatures at each speed. There are no significant stresses measured in torsion on the third stage rotor blades.

Combined Damping

The averaged output power spectra for the third-stage rotor blade instrumented with gage number 19 at the design equivalent speed is shown in figure 14a. The data was acquired with the stator blades set to the maximum efficiency schedule with the inlet pressure at 0.5 atm at the throttle position shown in figure 9. Figure 14a shows both engine order and non-synchronous responses. The engine order responses are periodic and are seen as spikes at all multiples of the rotational speed. The non- synchronous response outlines the first bending, first torsion, and second bending modes of the rotor blade. Figure 14b highlights the first torsion mode in figure 14a. Figure 14b also shows the SDOF transfer function fit to the data. The curve fit was performed to the data near the nonsynchronous peak between 3103 and 3165 Hz. The curve fit follows the data beyond the frequency range to which it was fit.

The SDOF transfer function describes the individual modes and establishes the undamped natural frequency and damping ratio. Graphical results of the curve fits for the third-stage rotor blades are presented in the Appendix. Data is presented at the design equivalent speed with the stators reset for maximum efficiency at the operating point shown in figure 9. Data is also presented at 70, 80, and 90 percent design equivalent speed with the stators at

their design setting angles at the operating points identified in figure 8. Tables 2 to 5 summarize the damping and natural frequency results.

Aerodynamic Damping

The aerodynamic damping ratio at the standard day inlet pressure is given by equation (37)

$$\zeta = \zeta_s + \zeta_{a,std} \left(\frac{P_{in}}{P_{std}} \right)$$

as the slope of the measured damping ratio variation with inlet total pressure. Figure 15 is the variation of the measured damping ratio with inlet total pressure for the third stage rotor blade first bending mode at design equivalent speed. The data was obtained with the variable vanes reset to the maximum efficiency positions. The compressor overall performance at this position is identified on figure 9. The measured damping ratios follow the linear relation. Also shown on figure 15 is a least squares approximation to equation (37)

$$\zeta = 0.00134 + 0.0120\ P_{in}/P_{std}$$

The aerodynamic damping is the greatest portion of the measured damping even at the lowest of the three inlet pressures.

The variation of the measured damping in the first torsion mode for the same operating conditions as figure 15 is shown in figure 16. Also shown is the least squares approximation of equation (37)

$$\zeta = -0.000326 + 0.00994\ P_{in}/P_{std}$$

The least squares fit results in a small negative nonaerodynamic damping. The structural and mechanical damping in the first torsion mode is anticipated to be small [4]. The difference between the negative value determined and the actual nonaerodynamic damping is realistically with the accuracy of the data. For the torsional mode as well as the bending mode the majority of the measured damping is aerodynamic.

The scatter at each inlet pressure in the measured damping in the first torsion mode is less than the scatter in the measured damping in the first bending mode at the design speed. In the first bending mode the scatter is of the same order of magnitude as the nonaerodynamic damping. Since the scatter is less in the first torsion mode where the nonaerodynamic damping is less and since the scatter is of the same order of magnitude as the nonaerodynamic damping in the first bending mode, the scatter in the data is attributed primarily to differences in the nonaerodynamic damping.

The measured damping in the first bending mode of the third stage rotor at 90 percent design equivalent speed is shown in figure 17. The data was acquired with the stators at their design positions and the throttle 90 percent open. The overall performance at this operating point is shown in figure 8. There is much more scatter in the data at the lowest and highest inlet pressures than at the 0.5 atm inlet pressure. The scatter at the 0.5 atm inlet pressure is of the same order as that measured at the design

speed. Shown on the figure is the least square approximation to equation (37)

$$\zeta = 0.00144 + 0.0118\ P_{in}/P_{std}$$

which was fit to the data excluding the data point with the highest damping at the highest inlet pressure.

The measured damping variation in the first torsion mode is shown in figure 18 for 90 percent speed. The data follows the trends shown by the torsion mode at the design speed. The scatter is greater at the highest inlet pressure. The least squares fit of equation (37)

$$\zeta = 0.000732 + 0.00684\ P_{in}/P_{std}$$

again excludes the data point with the highest damping at the highest inlet pressure. Here the majority of the damping is aerodynamic as it was at the design speed.

The variation of damping with inlet total pressure for the third-stage rotor first bending mode at eighty percent design equivalent speed is shown in figure 19. It is not possible to fit the SDOF transfer function to the data at the lowest inlet pressure from the blade instrumented with gage 19 due to the closeness of the excitation to the natural frequency. Since the mechanical speed is slightly different at the other inlet pressures the curve fits were performed successfully. Again scatter in the data is greatest at the extreme operating pressures. The least square approximation to equation (37)

$$\zeta = -0.00008 + 0.00148\ P_{in}/P_{std}$$

results in a small negative nonaerodynamic damping.

Damping variation in the first torsion mode at 80 percent speed is shown in figure 20. At the lowest inlet pressure it was not possible to define the damping measured with gage 19. A least squares fit is shown through the data

$$\zeta = -0.000466 + 0.00839\ P_{in}/P_{std}$$

The structural and mechanical damping is again determined to be negative.

At 70 percent design equivalent speed the third stage rotor blades resonated in the first bending mode. The resonant stress was most severe on the blade with gage 23 for each operating point. This is constant with the data in figures 11 to 13 which was acquired on a different test date. The natural frequency of the blade with gage 19 was close to the 7/rev excitation and the gage exhibited large stresses but less than those on the blade with gage 23. The blade with gage 17 responded to the 7/rev excitation only at the increased inlet pressure where the natural frequency changed from that at the two lower inlet pressures. This change in natural frequency is much greater than any to be expected from the pressure variation and remains unexplained. The measured damping is plotted in figure 21. No approximation to equation (37) is shown.

The damping in the first torsion mode for the blades with gages 17 and 19 are plotted in figure 22. The blade with gage 23

exhibits two distinct first torsion modes. Shown is the approximation of equation (37)

$$\zeta = -0.000122 + 0.00681\ P_{in}/P_{std}$$

The damping was measured at all the three inlet total pressures at the design equivalent speed prior to an extensive post-stall performance test. The damping was measured at the 0.5 atm inlet pressure at 80 and 90 percent speed prior to the install testing. The damping at the lowest and highest inlet pressures at 80 and 90 percent speed and the damping at all the inlet pressures at 70 percent speed were measured following much of the install testing. During the post-stall testing the compressor operating temperatures and stresses exceeded those during unstalled operation. Stresses and temperatures are monitored throughout testing to insure the integrity of the experimental hardware. After the post-stall performance testing their was no concern that additional damping measurements would not agree with those previously acquired.

Two obvious differences exist between the data acquired before and after the post-stall testing. Figures 23 to 25 show the natural frequencies determined for the three strain gaged third stage rotor blades. The natural frequencies for each of the three blades do not show much variation with inlet pressure at the design speed as is to be expected. The frequencies in the first bending mode at 80 and 90 percent speed with the 0.5 atm inlet pressure and the frequencies determined at the design speed all follow

$$f^2 = f_0^2 + c(rpm)^2 \qquad (39)$$

which is Southwell's theorem [22]. Shown in figures 23 and 24 is the least square approximation of equation (39) to the data acquired prior to the post-stall testing in the first bending mode. Shown in figure 25 is the least square fit of equation (39) to all the data acquired in the first bending mode. In each case equation (39) describes the variation in natural frequency with rotational speed. The data acquired after the post-stall testing shown in figures 23 and 24 is not explained by the anticipated frequency variation.

The variations in the first bending natural frequencies are not expected from aerodynamic considerations. Similar variations in the first torsion mode frequencies are also seen in figure 23. It is suggested the compressor rotor wheel, the rotor blades or the strain gages were damaged during the post-stall testing. The compressor rotor was disassembled after the experiment was competed. No anomalies were noted during the disassembly. The strain gaged rotor blades were removed from the rotor wheel. No appearance of damage was noted.

The second difference in the strain gage measurements is the appearance of an additional mode on the strain gage output power spectra. Figure 26a is the output power spectra for the strain gage number 17 on the third stage rotor blade at 90 percent design speed. The data was acquired prior to the install testing with the inlet pressure of 0.5 atm. Figure 26b is the data acquired at the reduced inlet pressure. The additional mode is seen between 2 and 3 kHz. Closer inspection reveals something in the same frequency

range in figure 14a which was also recorded prior to the post-stall testing. The additional mode is also seen on the first and second stage rotor blade data that is not shown which was recorded after the post-stall testing.

The cause of the additional mode seen after post-stall testing is also not presently available. It is speculated that the additional mode is due to the rotating data package since similar behavior is seen on all the rotor blade rows.

Because the scatter seen in the data acquired after the post-stall experiment was greater than that prior to the experiment, because of the variations in natural frequency measurements with inlet pressure where none were expected, and due to the appearance of the additional mode on the data, the aerodynamic damping determination at 70, 80, and 90 percent design equivalent speed is questioned.

The aerodynamic damping is successfully determined for the third-stage at the design equivalent speed in the first bending and first torsion modes. The aerodynamic damping is the largest portion of the damping at each of the inlet pressures tested. The aerodynamic damping is larger in the bending than the torsion mode. This is also seen at 70, 80, and 90 percent design equivalent speed where the data is less consistent. Determination of the structural and mechanical damping is also important by itself. Any prediction of flutter or forced response requires both the structural and mechanical damping and the aerodynamic damping be known.

Determination of the aerodynamic damping in a realistic high speed environment allows assessing unsteady aerodynamic models as well as guiding the design of future and growth compressors. Determination of the aerodynamic damping allows assessing forced response of a known compressor in different applications. High Mach number applications are of particular interest. High inlet stagnation pressures associated with high flight speed may encourage additional aeroelastic problems. So long as Reynolds number changes do not significantly effect the flows forcing the vibrations the alternating stress can be assessed with equation (38) knowing the damping variation with inlet pressure.

SUMMARY

The aerodynamic damping is determined from rotor blade strain gage output power spectra. A SDOF transfer function is fit to the peak of the power spectra in each mode. The transfer function describes the data and provides the combined damping ratio and natural frequency. By assuming the structural and mechanical damping do not vary with inlet pressure the aerodynamic damping is determined at constant corrected speed. Damping measurements at three inlet total pressures provide the aerodynamic and the structural and mechanical damping.

The aerodynamic damping is determined for the third stage rotor blade at the design speed in the first bending and first torsion modes. The aerodynamic component is the greatest portion of the combined damping at each of the three inlet pressures tested in both bending and torsion. The aerodynamic damping ratio in the first bending mode corresponding to a standard day inlet pressure is 0.0120. The aerodynamic damping ratio in the first torsion mode corresponding to the standard day inlet pressure is 0.00994. Scatter in the damping data correlate roughly to the nonaerodynamic damping in each mode.

Trends in the combined damping obtained at 70, 80, and 90 percent design equivalent speed agree with the data acquired at the design speed. However; the data obtained following an extensive post-stall experiment are much less consistant.

REFERENCES

1. Kielb, R. E.; Leissa, A. W.; and Macbain, J. C.: Vibrations of Twisted Cantilever Plates - A Comparison of Theoretical Results. Int. J. Numer. Methods Eng., vol. 21, no. 8, 1985, pp. 1365-1380.
2. Whitehead, D. S.: Force and Moment Coefficients for Vibrating Aerofoils in Cascade. British A.R.C. R & M-3254, Feb. 1960.
3. Thomson, W. T.: Vibration Theory and Applications. Third Edition, Prentice-Hall, New York, 1965.
4. Srinivasan, A. V.; Cutts, D. G.; and Sridhar, S.: Turbojet Engine Blade Damping. (REPT-R81-91441031, United Technologies Research Center; NASA Contract NAS3-21708) NASA CR-165406, 1981.
5. Bisplinghoff, R. L.; Ashley, H.; Halfman, R. L.: Aeroelasticity. Addison-Wesley Publishing Company, New York, 1955.
6. Carta, F. O.: Aeroelasticity and Unsteady Aerodynamics. The Aerothermodynamics of Aircraft Gas Turbine Engines, G. C. Oates, ed., AFAPL-TR-78-52, July 1978, Chapter 22. (Avail. NTIS, AD-A059784).
7. Platzer, M. F.; and Carta, F. O.: Aeroelasticity in Axial-Flow Turbomachines, vol. 1: Unsteady Turbomachinery Aerodynamics, AGARD-AG-298-VOL-1, AGARD, Neuilly-Sur-Seine, France, 1987. (Avail. NTIS, AD-A181676).

8. Crawley, E. F.: Measurements of Aerodynamic Damping in the MIT Transonic Rotor. (GTL-157, Massachusetts Institute of Technology; NASA Grant NSG-3079.) NASA CR-163988, 1981.

9. Fung, Y. C.: An Introduction to the Theory of Aeroelasticity. Dover Publications, New York, 1969.

10. Dowell, E. H., ed.: A Modern Course in Aeroelasticity. Sijthoff and Noordhoff, 1980.

11. Harker, R. J.: Generalized Methods of Vibration Analysis. John Wiley and Sons, New York, 1983.

12. Steinke, R. J.: Design of 9.271-Pressure-Ratio Five-Stage Core Compressor and Overall Performance for First Three Stages. NASA TP-2597, 1986.

13. Cunnan, W. S.; Stevens, W.; and Urasek, D. C.: Design and Performance of a 427-Meter-per-Second-Tip-Speed Two-Stage Fan Having a 2.40 Pressure Ratio. NASA TP-1314, 1978.

14. Lesco, D. J.; Sturman, J. C.; and Nieberding, W. C.; On-The-Shaft-Data Systems for Rotating Engine Components. NASA TM X-68112, 1972.

15. Irving, I. A.; and Bullock, R. O., eds.: Aerodynamic Design of Axial-Flow Compressors. NASA SP-36, 1965.

16. Horlock, J. H.: Axial Flow Compressors. Robert E. Krieger Publishing Co., Huntington, NY, 1973.

17. Fluid Meters: Their Theory and Application. Fifth Edition, American Society of Mechanical Engineers, New York, 1959.

18. Glawe, G. E.; Holanda, R.; and Krause, L. N.: Recovery and Radiation Corrections and Time Constants of Several Sizes of Shielded and Unshielded Thermocouple Probes for Measuring Gas Temperature. NASA TP-1099, 1978.

19. Bendat, J. S.; and Piersol, A. G.: Random Data: Analysis and Measurement Procedures. Wiley-Interscience, New York, 1971.

20. Bendat, J. S.; and Piersol, A. G.: Engineering Applications of Correlation and Spectral Analysis. Wiley-Interscience, New York, 1980.

21. James, M. L.: Smith, G. M.; and Wolford, J. C.: Applied Numerical Methods for Digital Computation with Fortran and CSMP. Second Edition, Harper & Row, New York, 1977.

22. Den Hartog, J. P.: Mechanical Vibrations. McGraw-Hill, New York, 1956.

TABLE 1. - MAXIMUM EFFICIENCY IGV-STATOR SETTING ANGLES

Percent design equivalent speed	Reset angles, degrees			
	IGV	Stator 1	Stator 2	Stator 3
50	29	10	2	-8
70	21	10	0	-8
80	18	10	0	0
90	15	6	2	0
100	0	10	6	10

TABLE 2. - THIRD-STAGE ROTOR BLADE COMBINED DAMPING RATIO AT DESIGN EQUIVALENT SPEED

Gage	Inlet Pressure, P_{in}/P_{std}	RPM	First bending		First Torsion	
			f_n, Hz	ζ	f_n, Hz	ζ
17	0.366	16104	1308	0.00634	3147	0.00349
	.505	16104	1312	.00816	3146	.00457
	.760	15918	1302	.0116	3144	.00738
19	.366	16098	1318	.00531	3133	.00358
	.505	16116	1322	.00759	3130	.00457
	.760	15912	1323	.00957	3132	.00686
23	.366	16098	1384	.00559	3295	.00324
	.505	16116	1389	.00648	3290	.00435
	.761	15912	1404	.0103	3302	.00765

TABLE 3. - THIRD-STAGE ROTOR BLADE COMBINED DAMPING RATIO AT 90 PERCENT DESIGN EQUIVALENT SPEED

Gage	Inlet Pressure, P_{in}/P_{std}	RPM	First bending		First Torsion	
			f_n, Hz	ζ	f_n, Hz	ζ
17	0.349	14136	1348	0.00733	3365	0.00336
	.503	14634	1285	.00810	3149	.00430
	.754	14136	1298	.0148	3239	.00906
19	.349	14124	1245	.00481	3143	.00316
	.503	14652	1297	.00688	3136	.00403
	.754	14136	1256	.0107	3142	.00592
23	.349	14130	1353	.00451	3325	.00269
	.504	14652	1386	.00711	3312	.00444
	.754	14136	1366	.00994	3325	.00577

TABLE 4. - THIRD-STAGE ROTOR BLADE COMBINED DAMPING RATIO AT 80 PERCENT DESIGN EQUIVALENT SPEED

Gage	Inlet Pressure, P_{in}/P_{std}	RPM	First bending		First Torsion	
			f_n, Hz	ζ	f_n, Hz	ζ
17	0.359	12595	1339	0.00627	3393	0.00247
	.509	12990	1260	.00729	3168	.00438
	.825	12574	1294	.0128	3328	.00735
19	.349	12597				
	.509	13009	1263	.00730	3147	.00388
	.825	12571	1260	.0138		
23	.349	12595	1320	.00436	3334	.00220
	.509	12986	1323	.00717	3315	.00353
	.825	12566	1336	.0101	3339	.00543

TABLE 5. - THIRD-STAGE ROTOR BLADE COMBINED DAMPING RATIO AT 70 PERCENT DESIGN EQUIVALENT SPEED

Gage	Inlet Pressure, P_{in}/P_{std}	RPM	First bending		First Torsion	
			f_n, Hz	ζ	f_n, Hz	ζ
17	0.355	11022	1336	0.00567	3414	0.00205
	.506	11028	1328	.0103	3410	.00290
	.864	11046	1286	.0119	3367	.00596
19	.355	11022			3341	.00309
	.506	11022	1273	.00812	3334	.00296
	.864	11040	1270	.00975	3313	.00579
23	.355	11016				
	.506	11028				
	.864	11034				

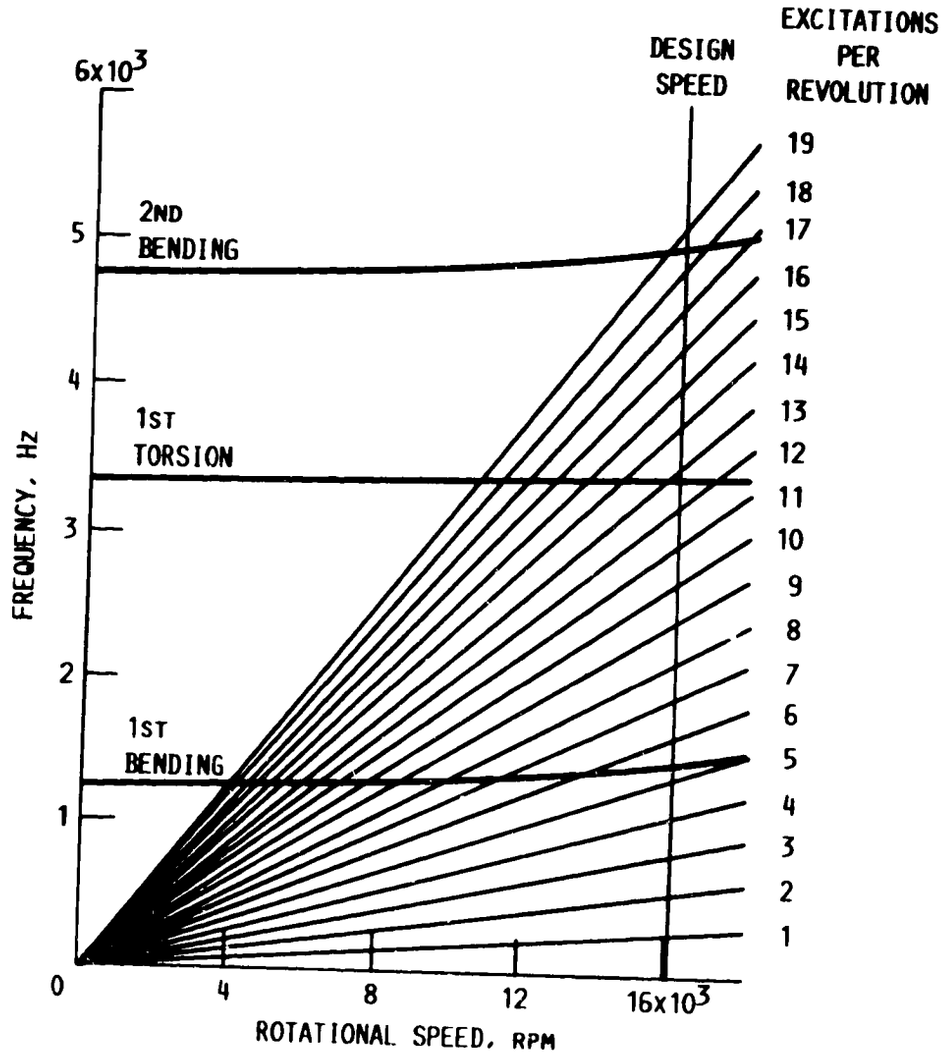

Figure 1 - Third-stage rotor blade Campbell diagram.

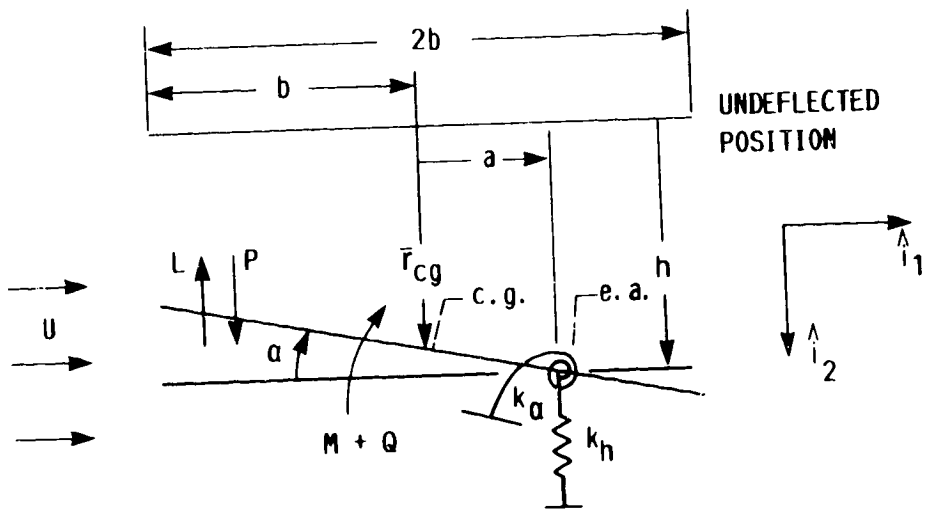

Figure 2 - Flat plate airfoil notation. (Structural and mechanical damping not shown.)

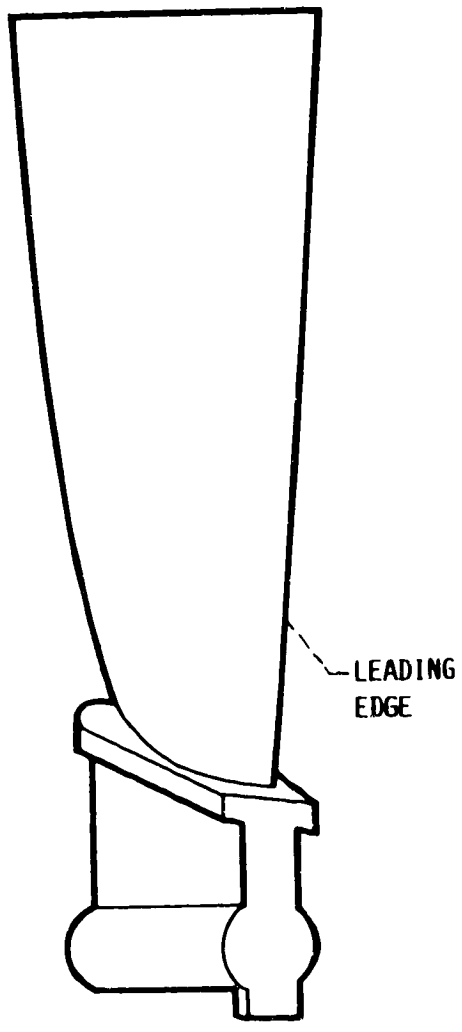

Figure 3 - Compressor rotor blade looking downstream along axis of rotation. (Not to scale.)

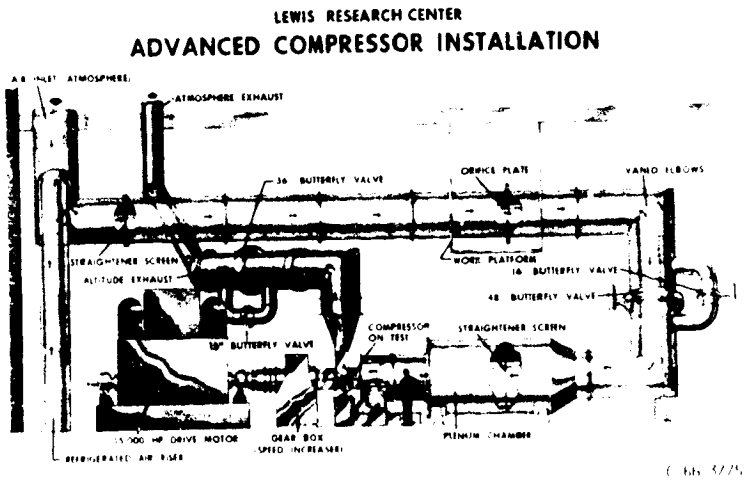

Figure 4 - Multistage compressor test facility.

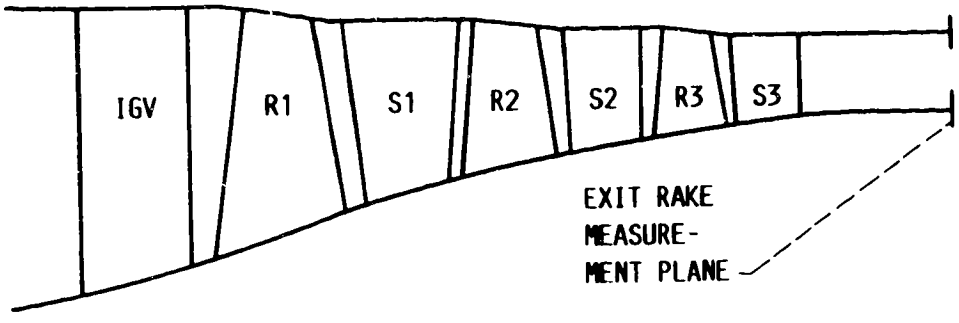

Figure 5 - Flowpath for first three stages of compressor 74B.

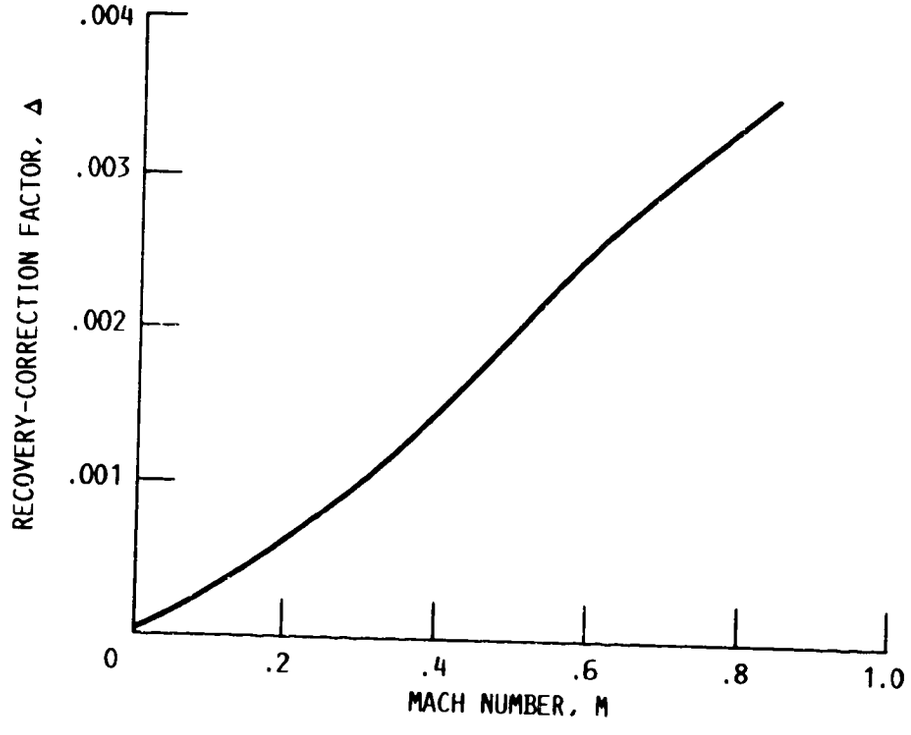

Figure 6 - Total temperature recovery-correction factor variation with Mach number for five-element exit total temperature and total pressure rakes.

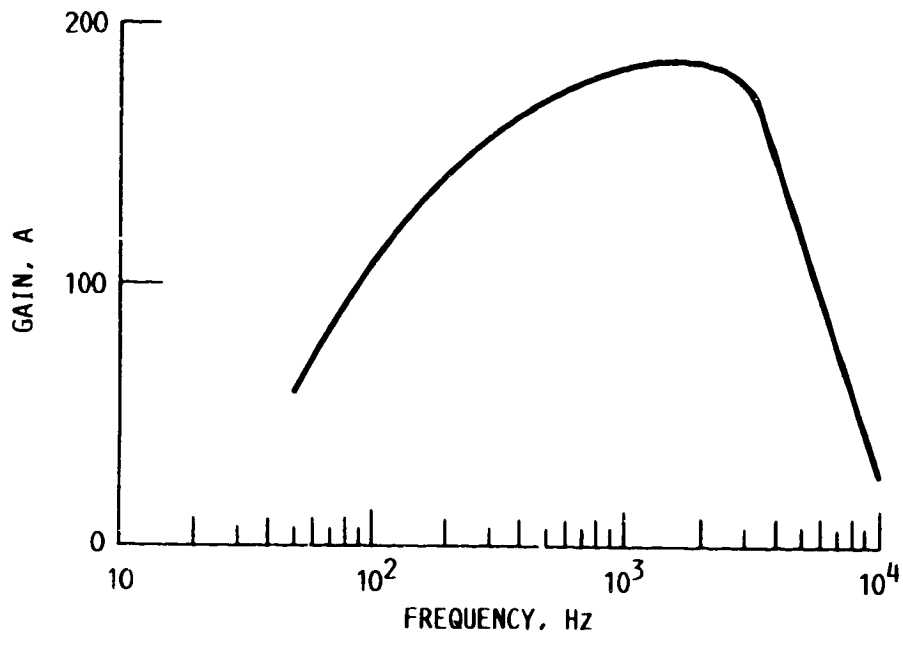

Figure 7 - Rotating strain gage data package gain.

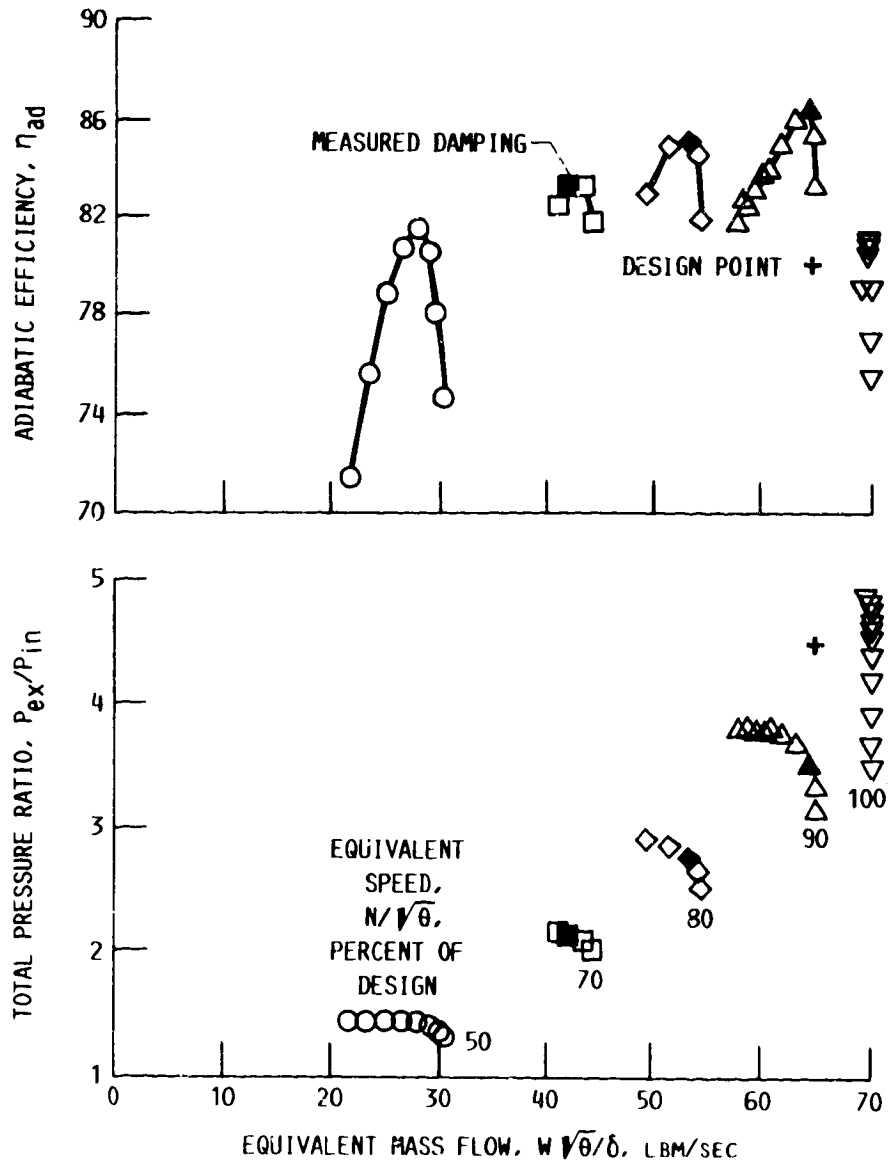

Figure 8 - Performance of first three stages of compressor 74B at design IGV-stator setting angles.

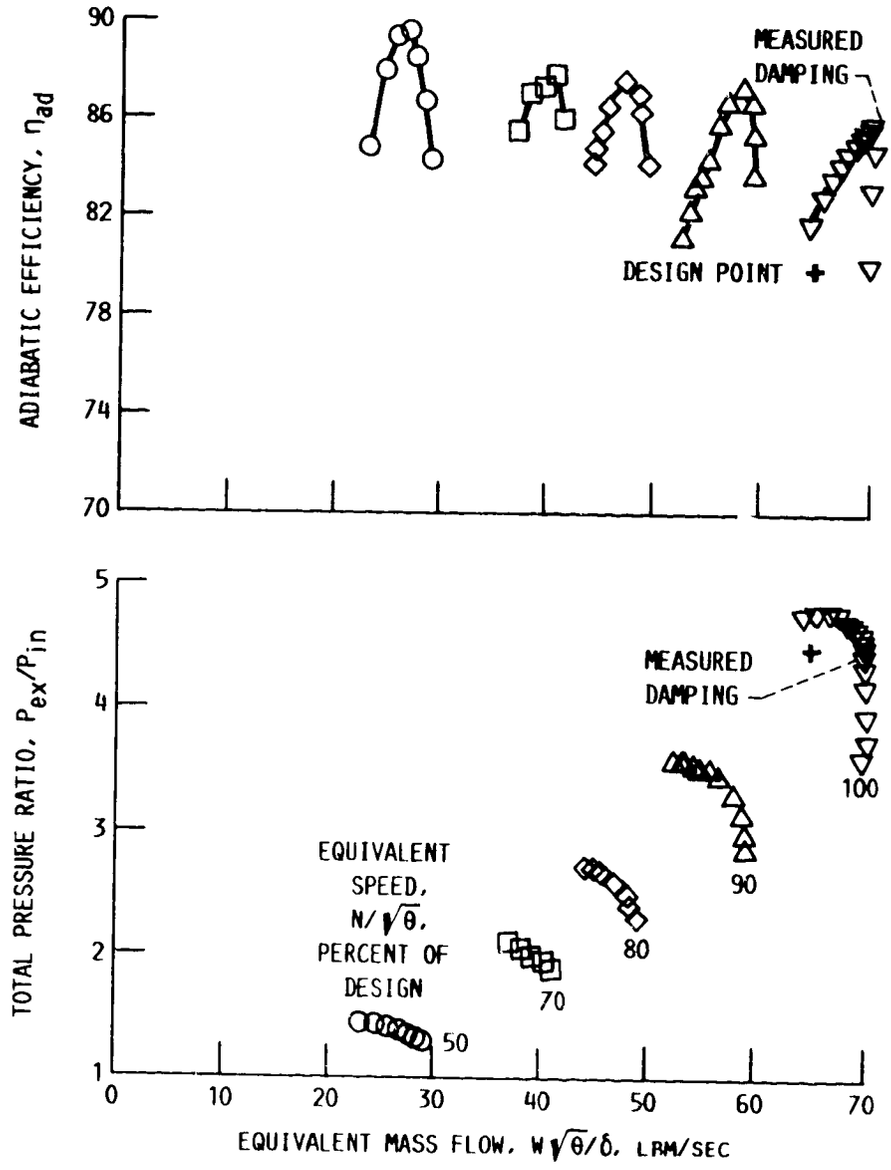

Figure 9 - Performance of first three stages of compressor 74B at maximum efficiency IGV-stator setting angles at each speed shown.

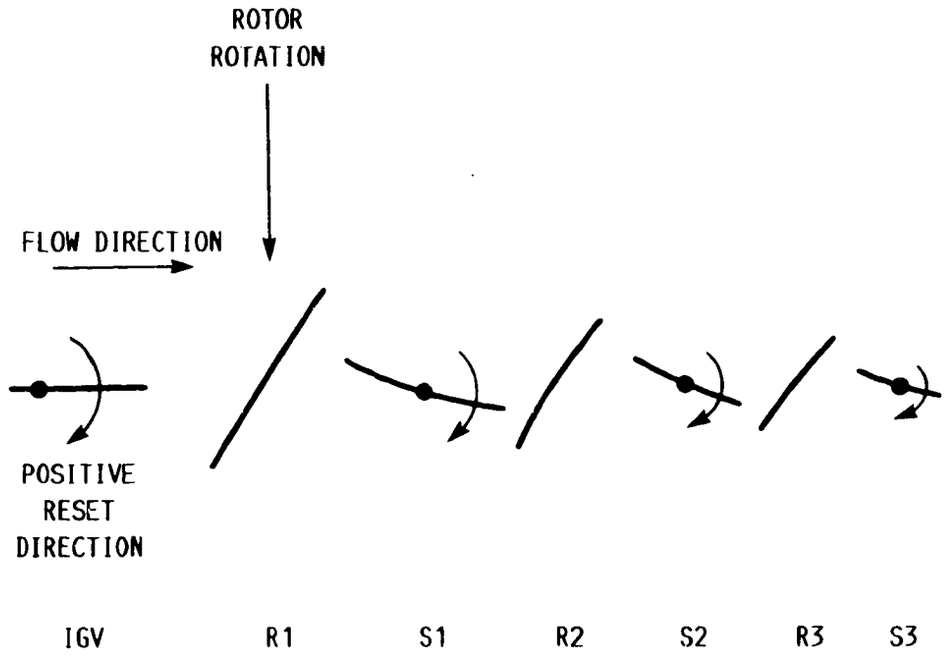

Figure 10 - Schematic of blade rows with positive direction of vane reset specified.

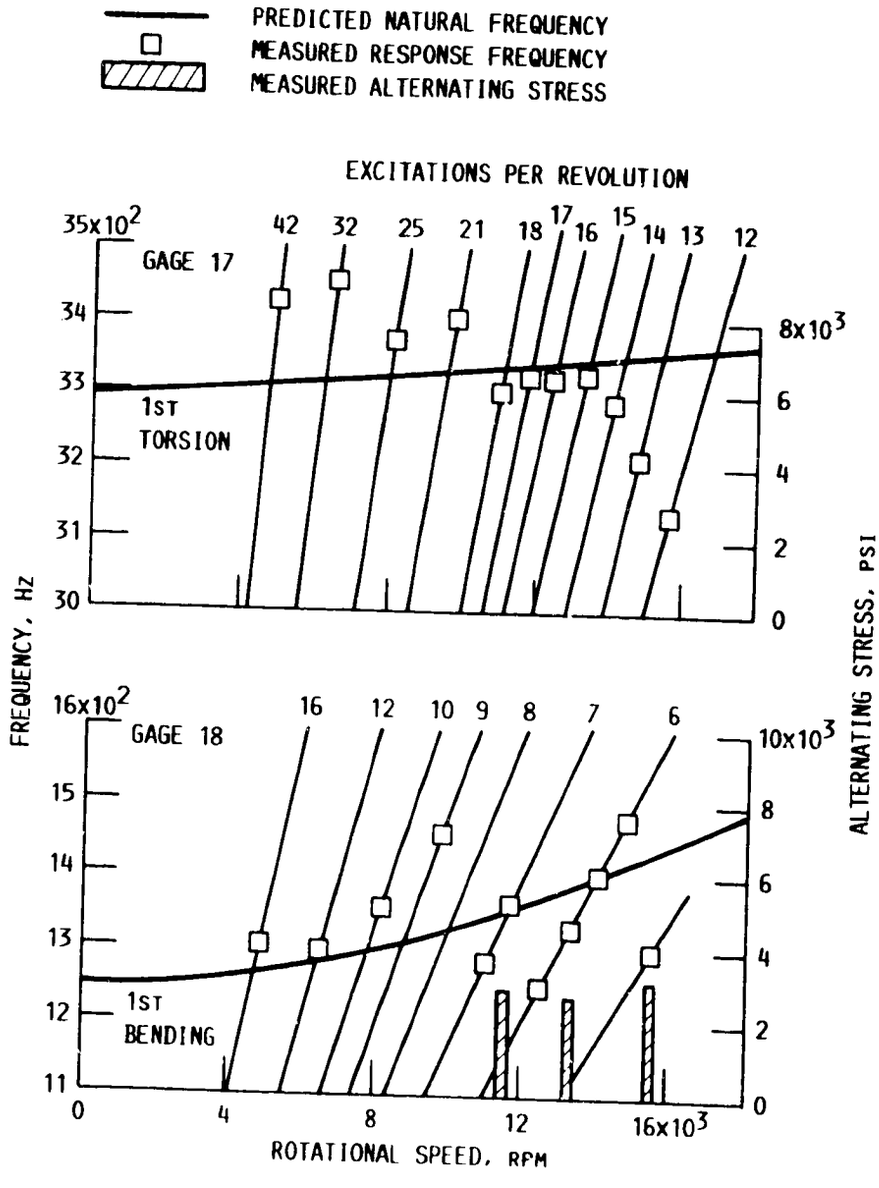

Figure 11 - Experimental Campbell diagram with alternating stress levels for third-stage rotor blade instrumented with gages 17 and 18. (Only measured stresses above 500 psi shown.)

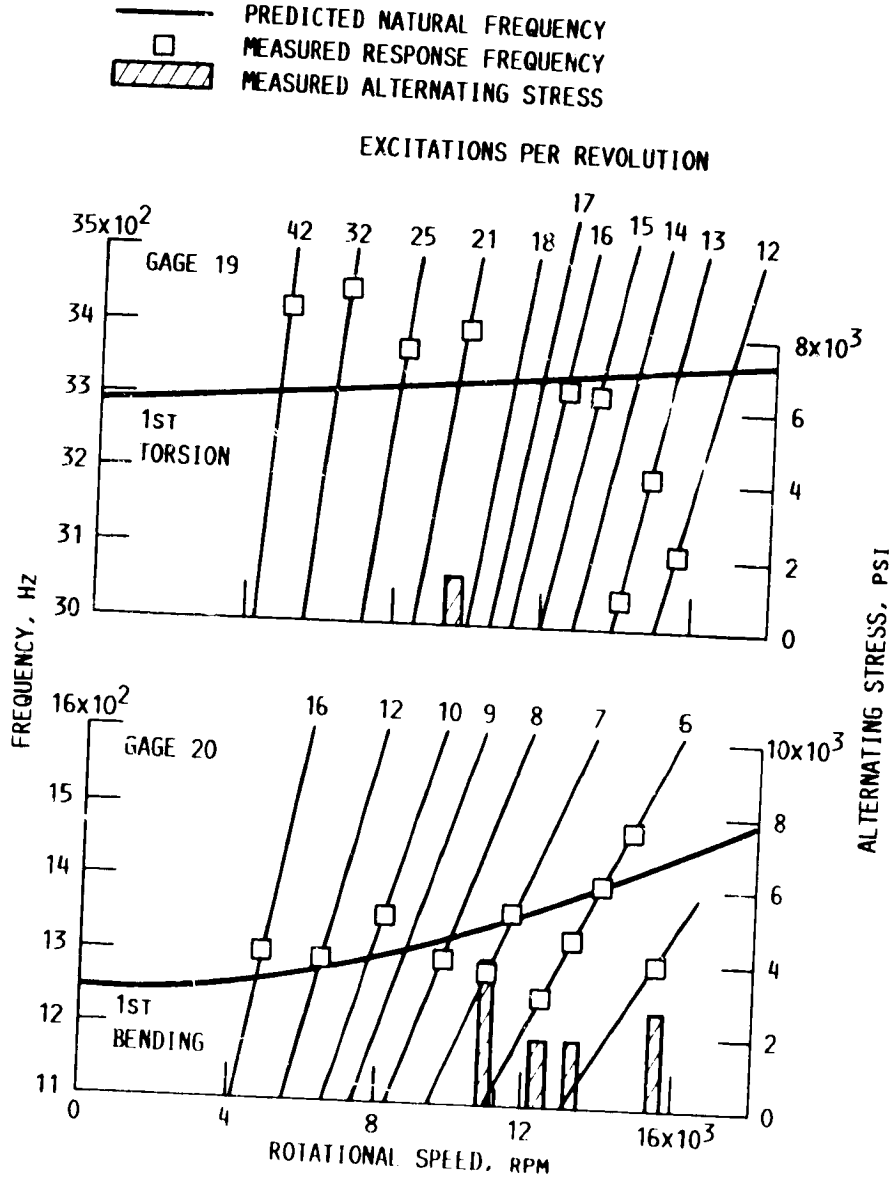

Figure 12 - Experimental Campbell diagram with alternating stress levels for third-stage rotor blade instrumented with gages 19 and 20. (Only measured stresses above 500 psi shown.)

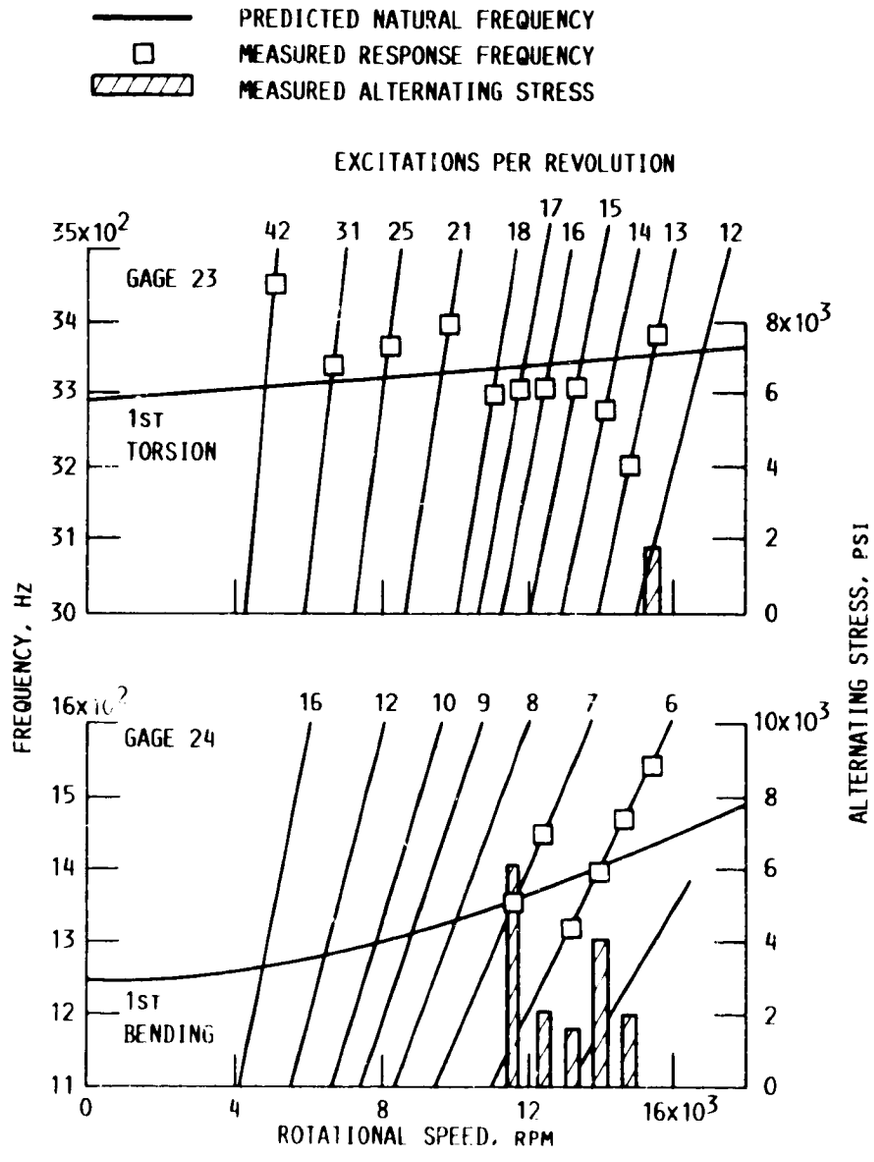

Figure 13 - Experimental Campbell diagram with alternating stress levels for third stage rotor blade instrumented with gages 23 and 24. (Only measured stresses above 500 psi shown.)

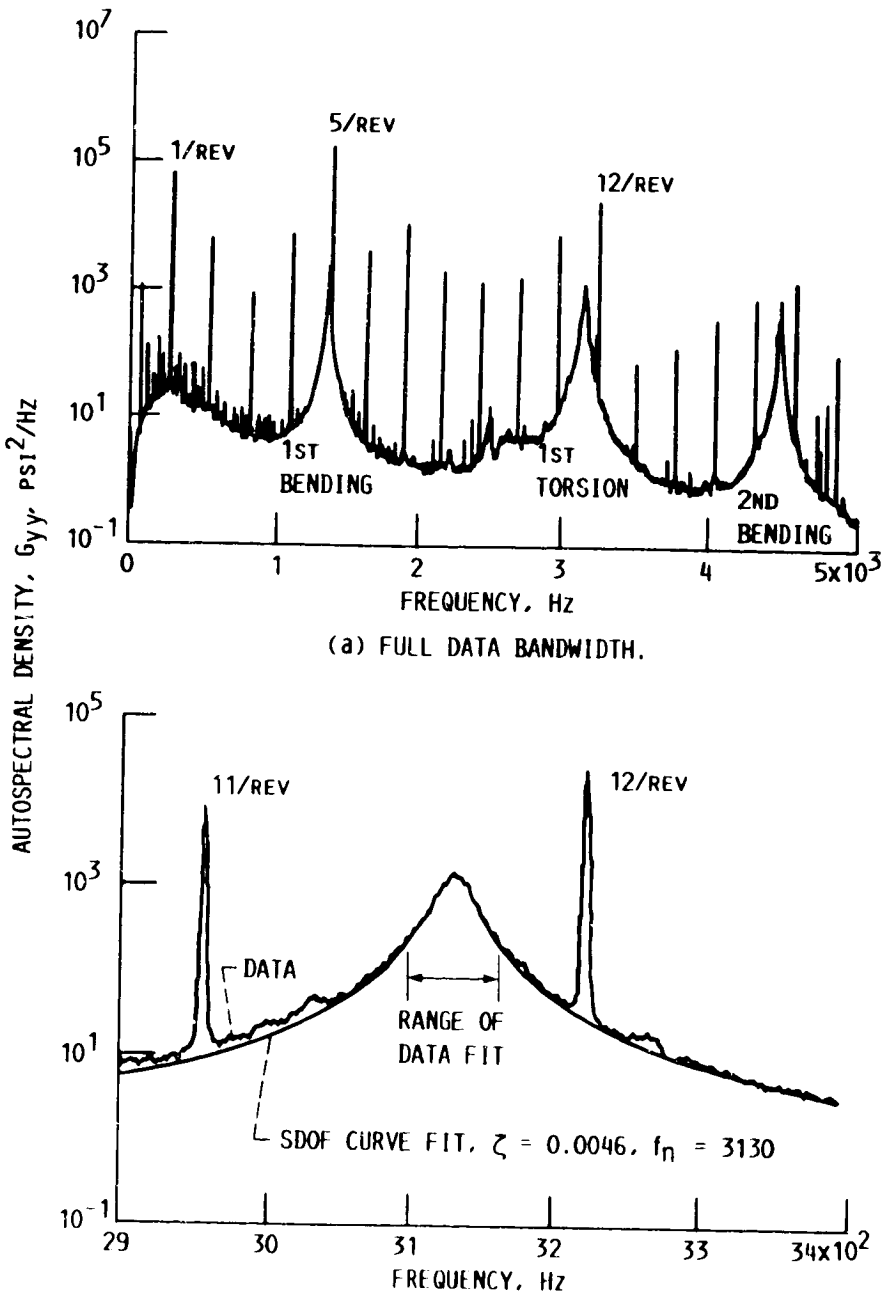

Figure 14 - Rotor three strain gage 19 output power spectra at design equivalent speed with IGV-stator setting angles at maximum efficiency positions and 1/2 atm inlet total pressure. (a) Full data bandwidth. (b) 1st torsion mode and SDOF curve fit.

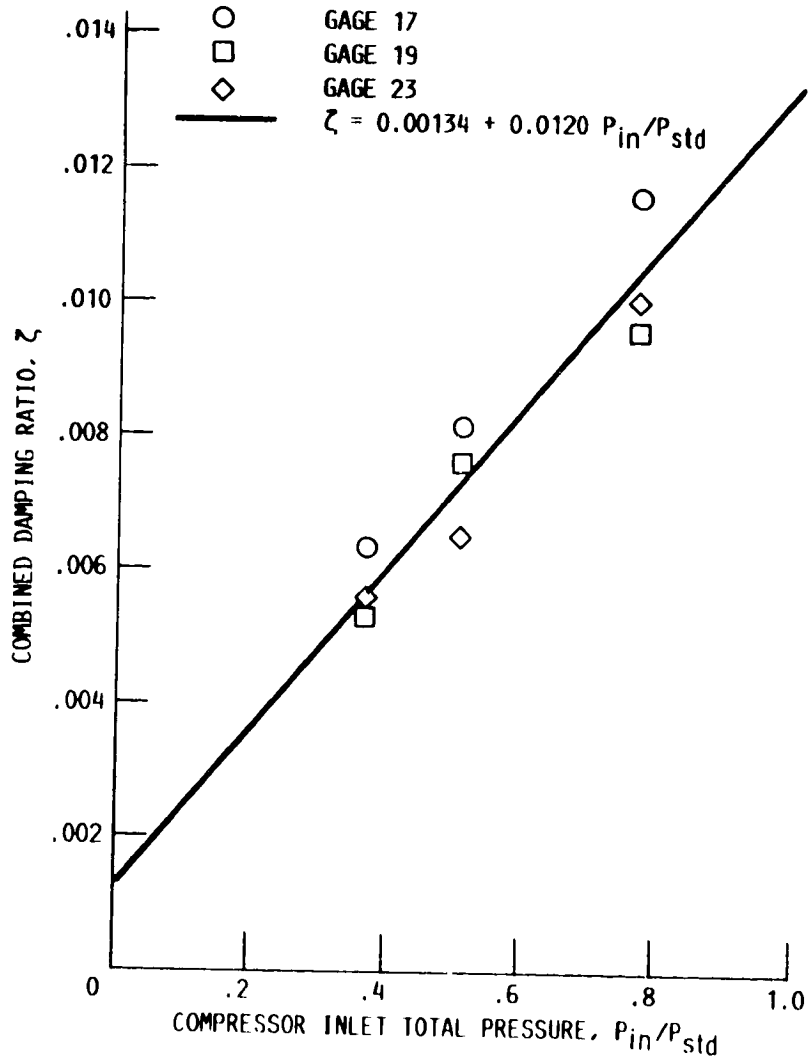

Figure 15 - Rotor three first bending mode combined damping ratio variation with inlet total pressure at design equivalent speed with IGV-stator setting angles at maximum efficiency positions.

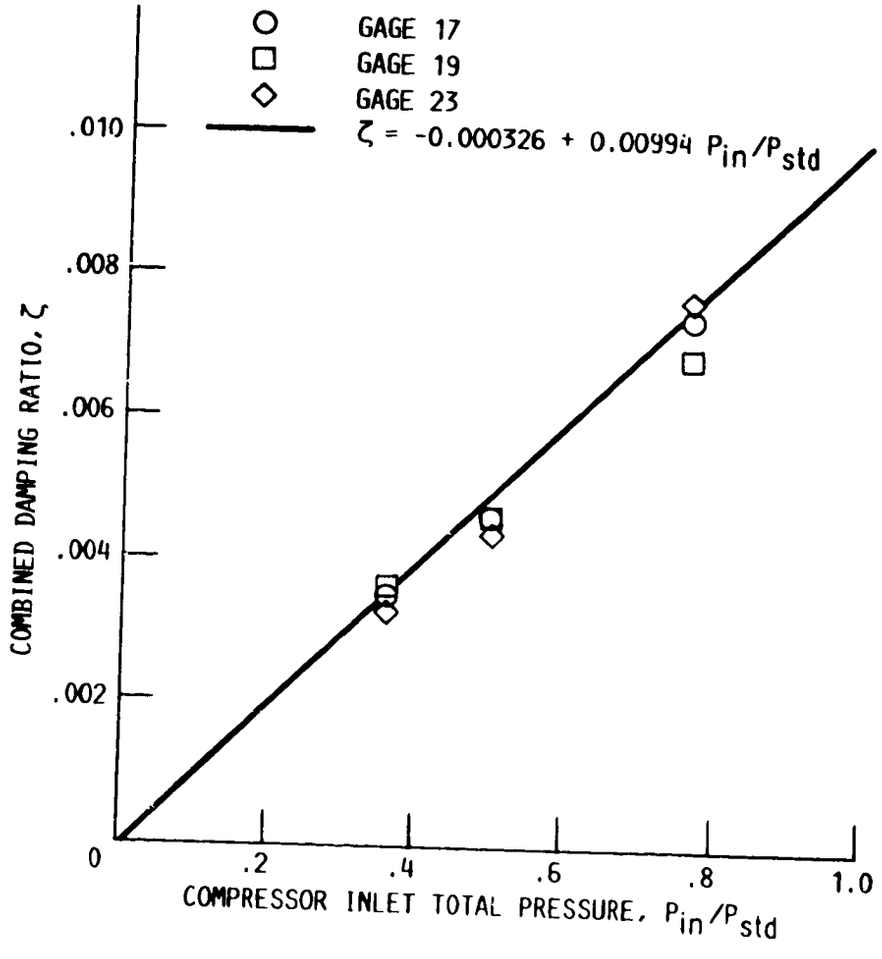

Figure 16 - Rotor three first torsion mode combined damping ratio variation with inlet total pressure at design equivalent speed with IGV-stator setting angles at maximum efficiency positions.

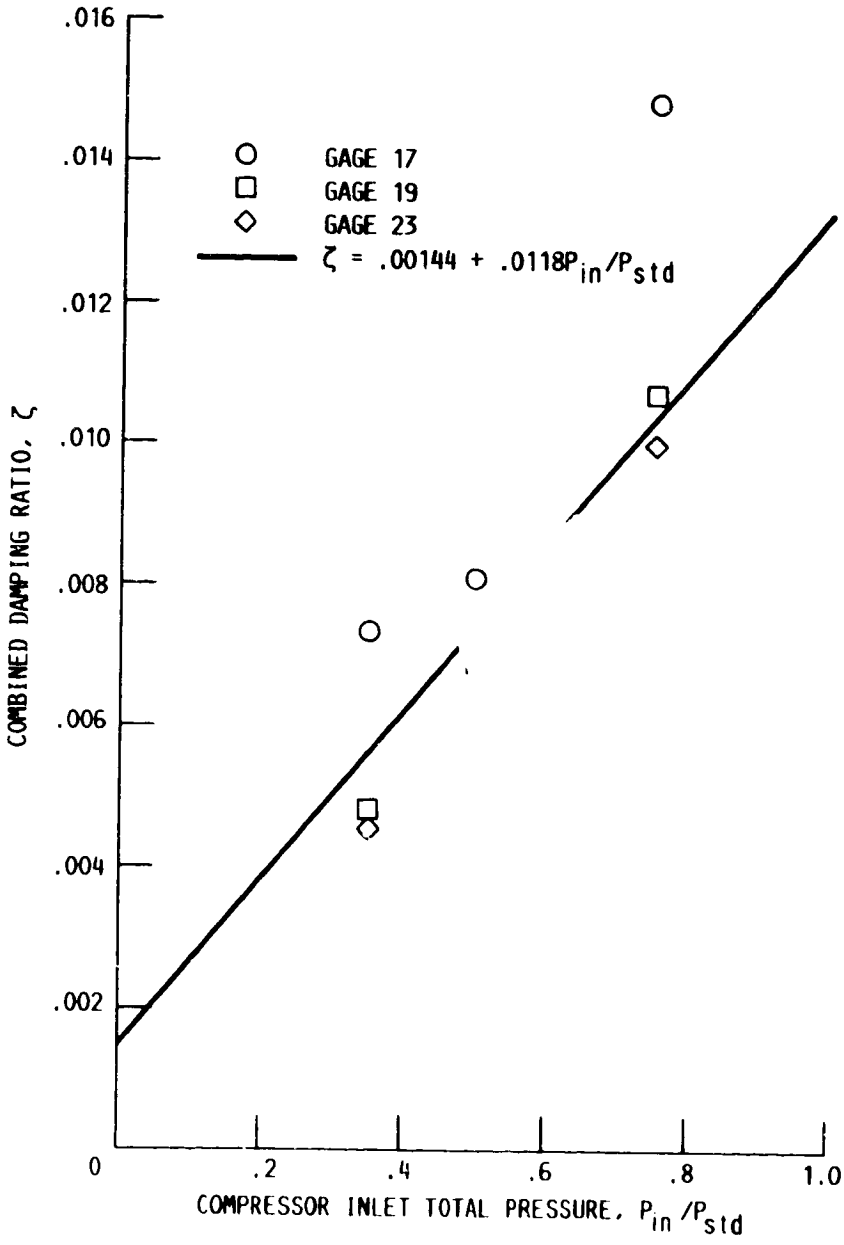

Figure 17 - Rotor three first bending mode combined damping ratio variation with inlet total pressure at 90 percent design equivalent speed with design IGV-stator setting angles.

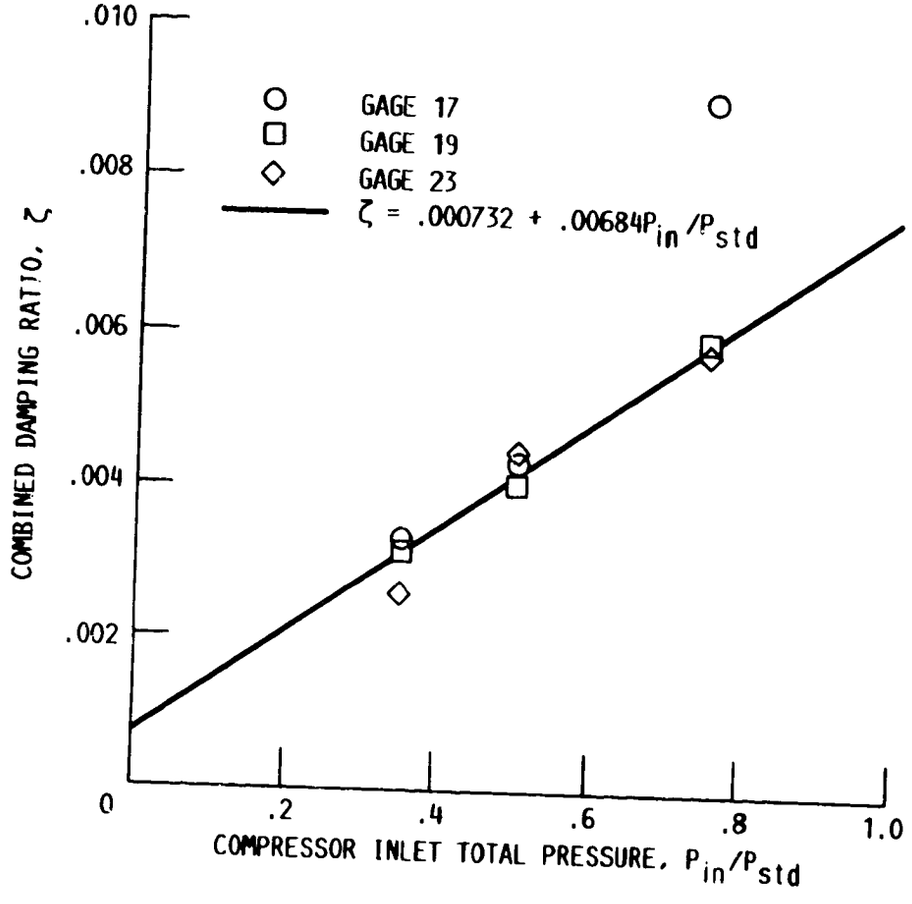

Figure 18 - Rotor three first torsion mode combined damping ratio variation with inlet total pressure at 90 percent design equivalent speed with design IGV-stator setting angles.

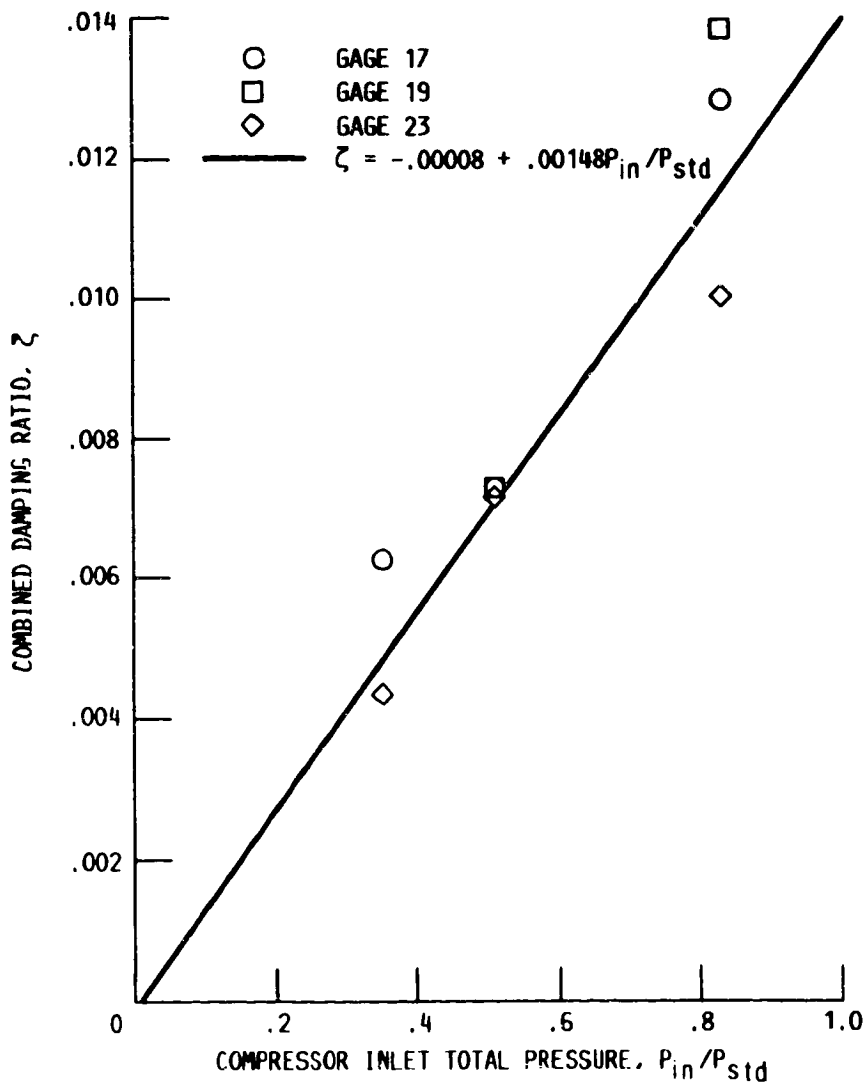

Figure 19 - Rotor three first bending mode combined damping ratio variation with inlet total pressure at 80 percent design equivalent speed with design IGV-stator setting angles.

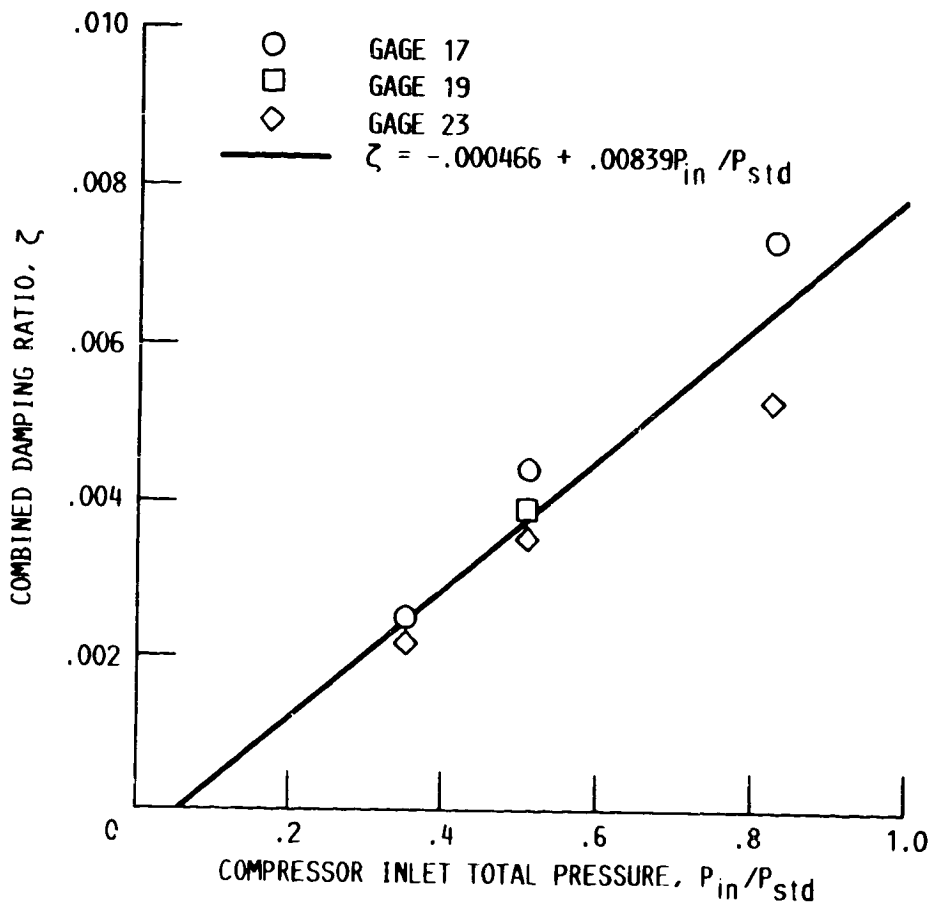

Figure 20 - Rotor three first torsion mode combined damping ratio variation with inlet total pressure at 80 percent design equivalent speed with design IGV-stator setting angles.

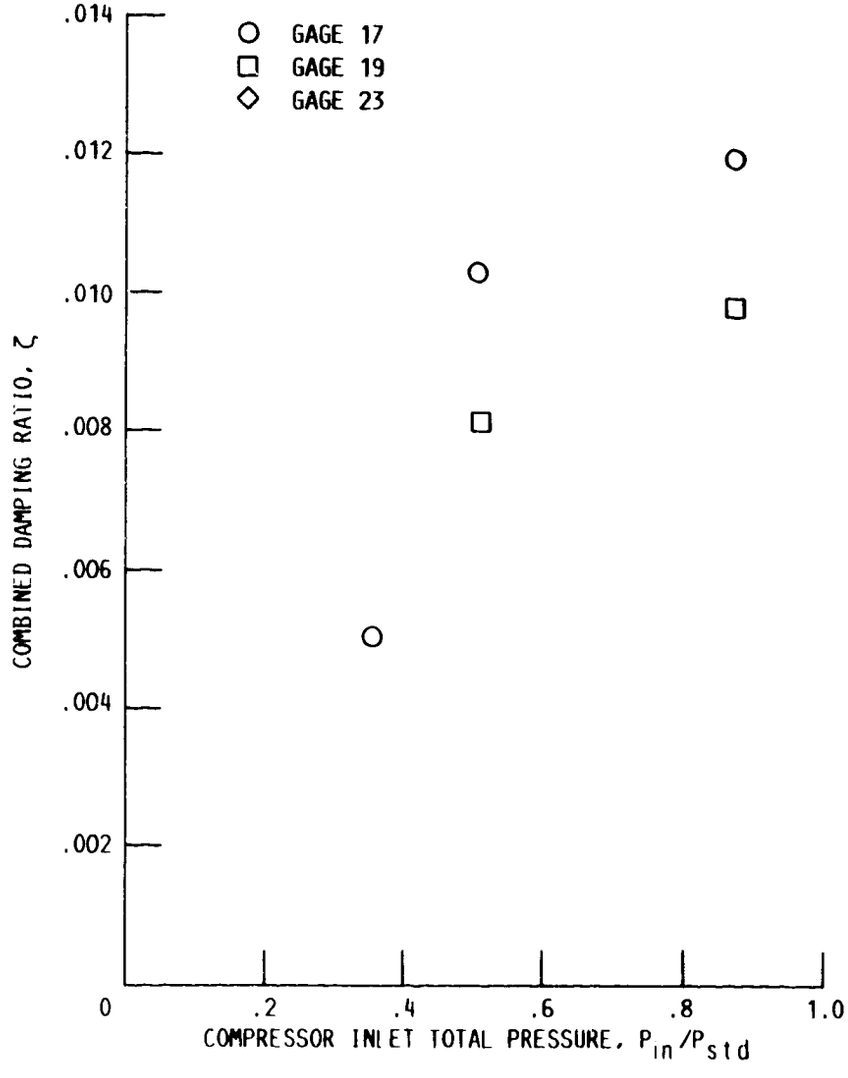

Figure 21 - Rotor three first bending mode combined damping ratio variation with inlet total pressure at 70 percent design equivalent speed with design IGV-stator setting angles.

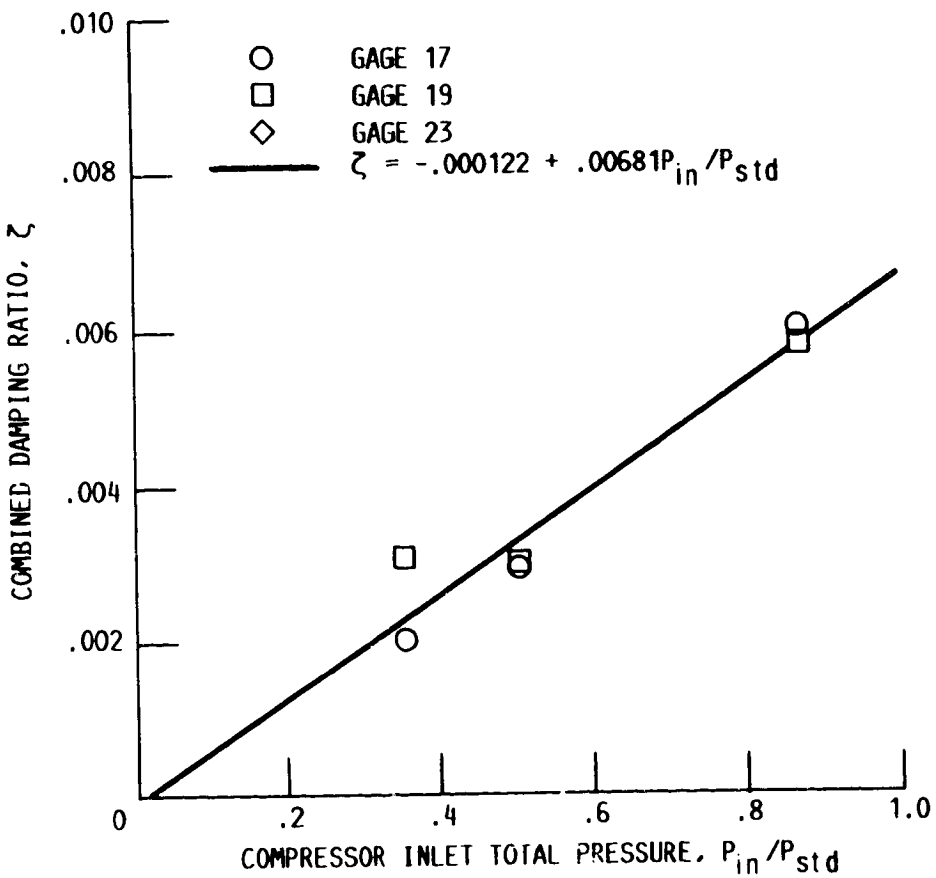

Figure 22 - Rotor three first torsion mode combined damping ratio variation with inlet total pressure at 70 percent design equivalent speed with design IGV-stator setting angles.

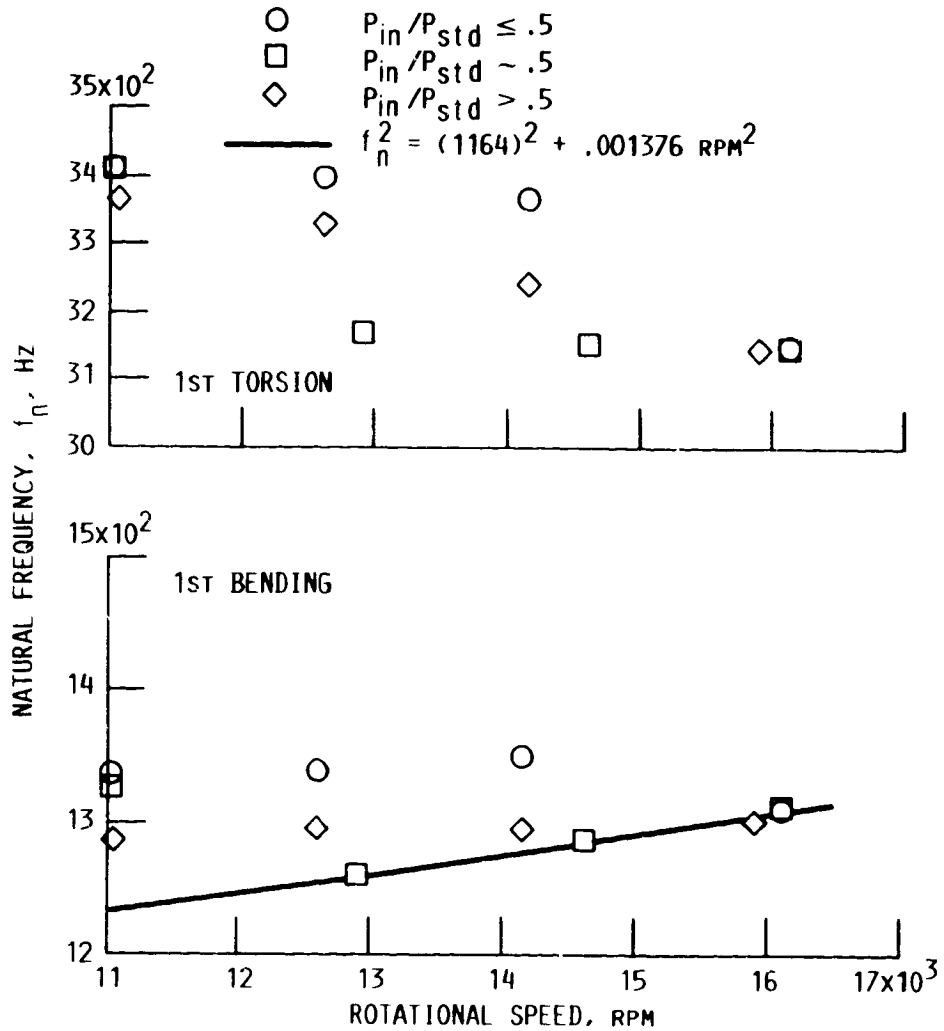

Figure 23 - Measured natural frequency variation with rotational speed for third-stage rotor blade instrumented with gage 17.

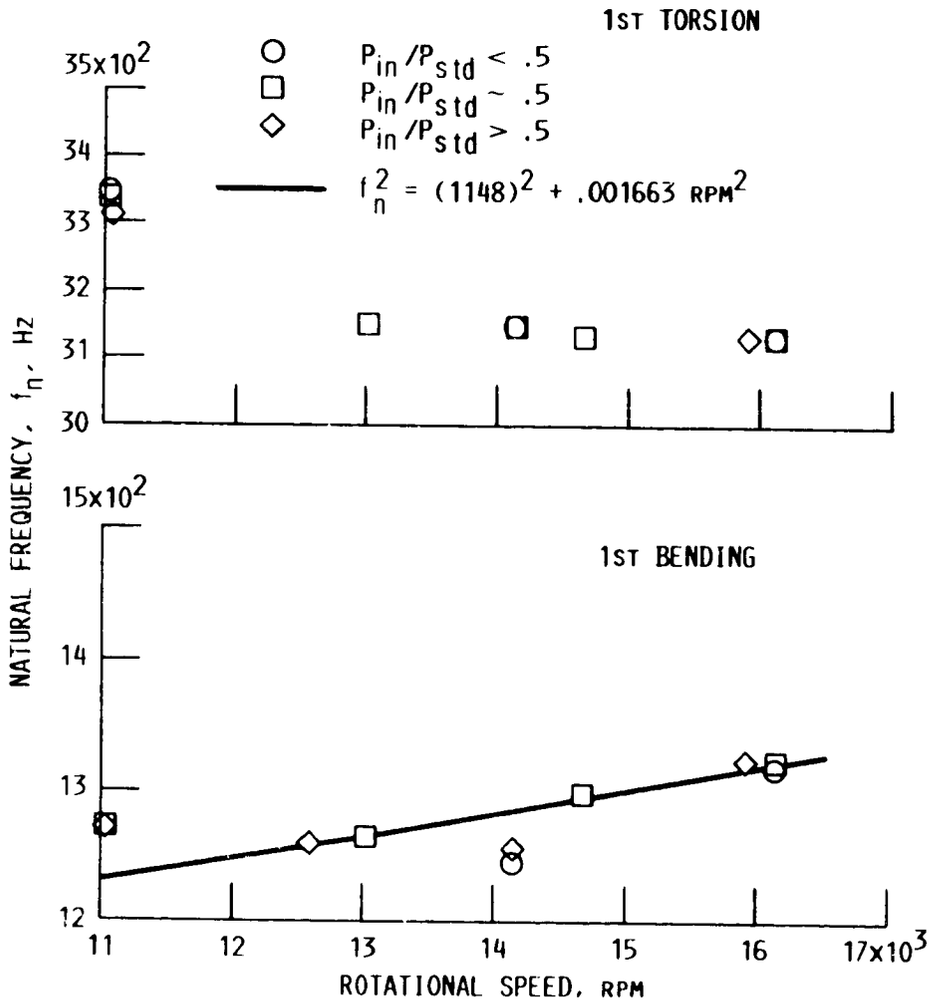

Figure 24 - Measured natural frequency variation with rotational speed for third-stage rotor blade instrumented with gage 19.

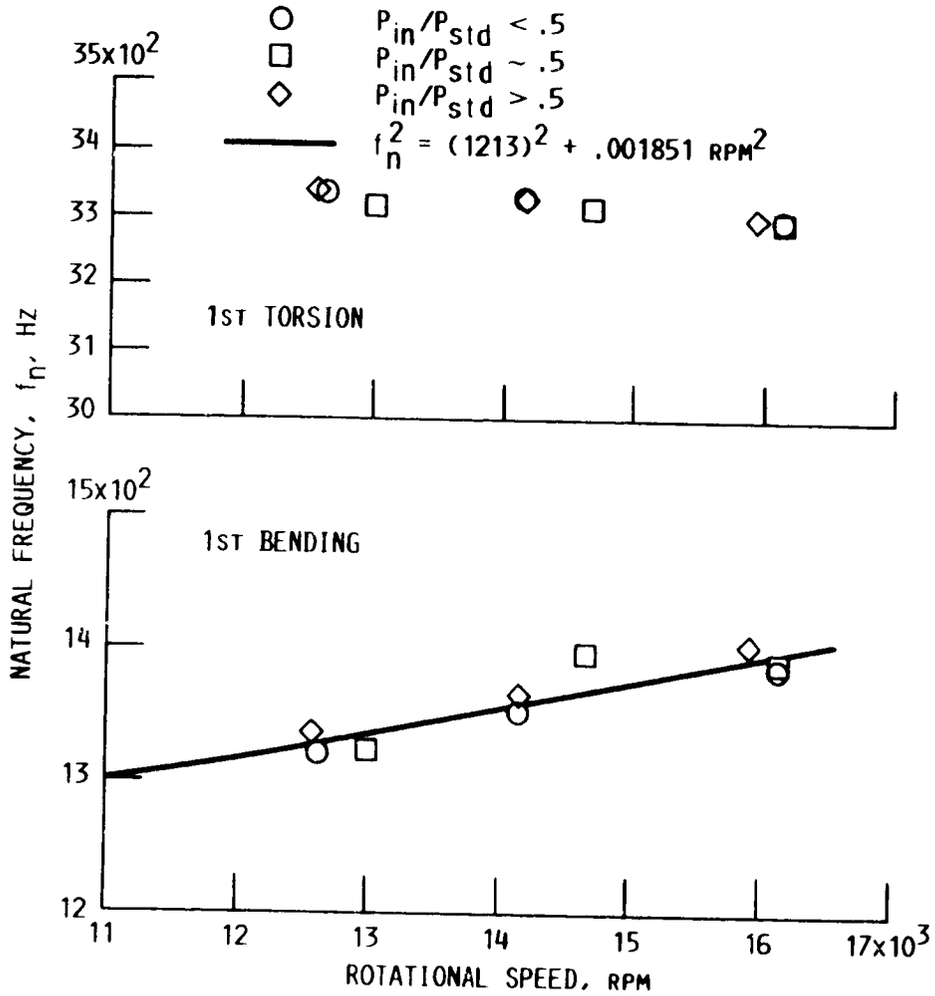

Figure 25 - Measured natural frequency variation with rotational speed for third-stage rotor blade instrumented with gage 23.

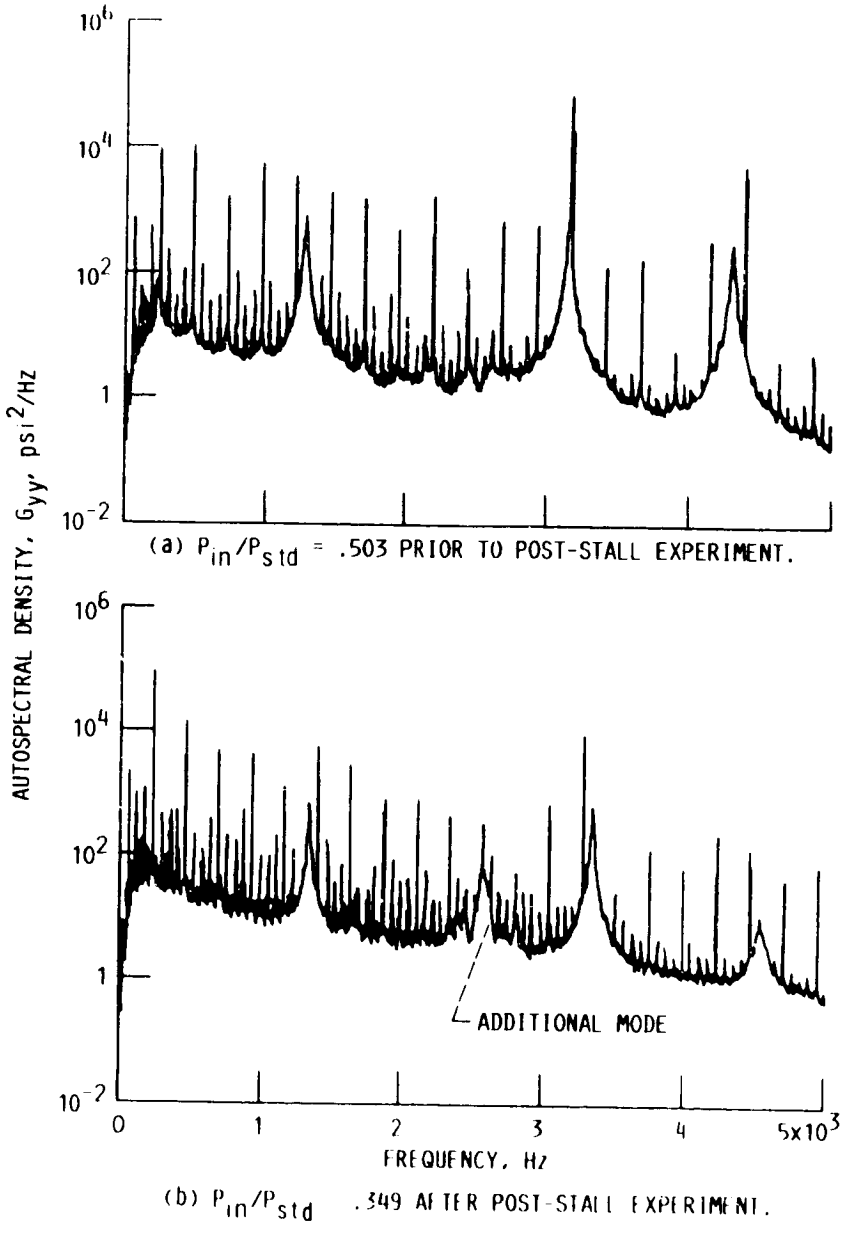

Figure 26 - Third-stage rotor blade strain gage 17 power spectra at 90 percent design equivalent speed.

APPENDIX

The SDOF curve fits used to determine the combined damping for the third-stage rotor blades are collected in the appendix. Each figure presents the first bending or first torsion mode at each of the three inlet pressures tested at each of 70, 80, 90, and 100 percent design equivalent speed. At 70, 80, and 90 percent design equivalent the variable IGV-stator setting angles are in their design position. At the design speed the IGV-stator setting angles are at the design speed maximum efficiency position.

Each figure shows the SDOF curve fit to determine the natural frequency and damping in each mode. Above the upper right-hand corner of each box is the natural frequency and damping ratio of the SDOF transfer function. Inside the box in the upper left-hand corner are the range of frequencies used in the curve fits. If two frequencies are listed, X1 and X2, the range of frequencies used are continuous. If four frequencies are displayed, two separate ranges, X_1-X2 and X3-X4, are used. In some instances it is not possible to obtain a satisfactory curve fit. In these cases the data is displayed alone.

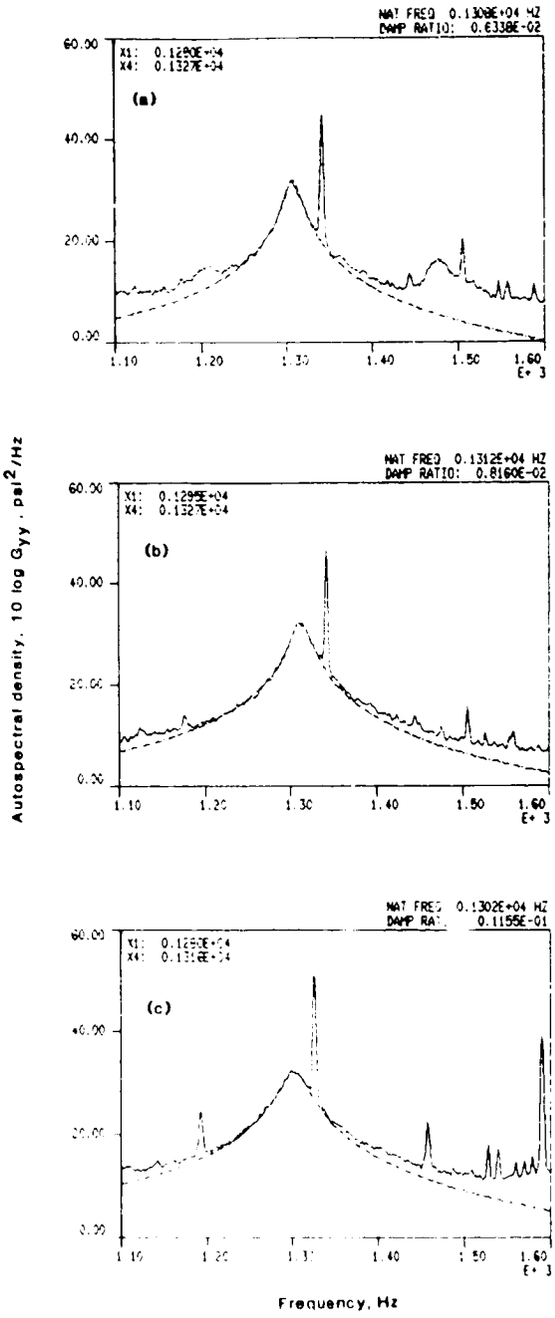

Figure A.1 - Rotor three first bending mode measured with gage 17 at design equivalent speed with maximum efficiency IGV-stator setting angles. Inlet total pressure/standard pressure (a) 0.366, (b) 0.505, (c) 0.760.

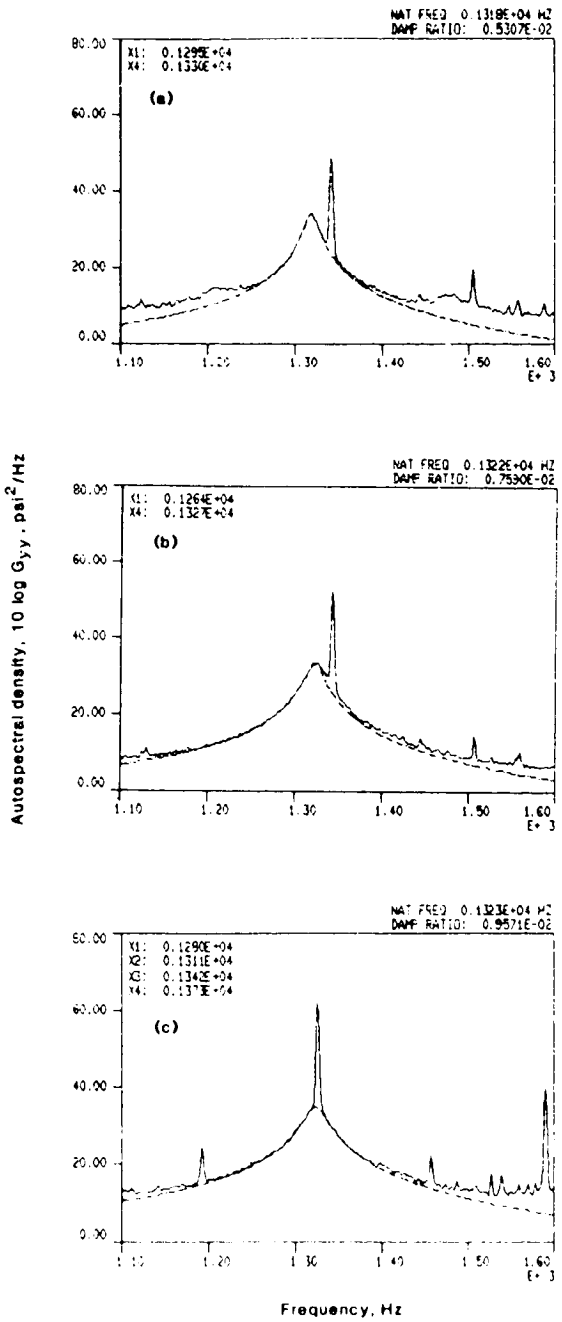

Figure A.2 - Rotor three first bending mode measured with gage 19 at design equivalent speed with maximum efficiency IGV-stator setting angles. Inlet total pressure/standard pressure (a) 0.366, (b) 0.505, (c) 0.760.

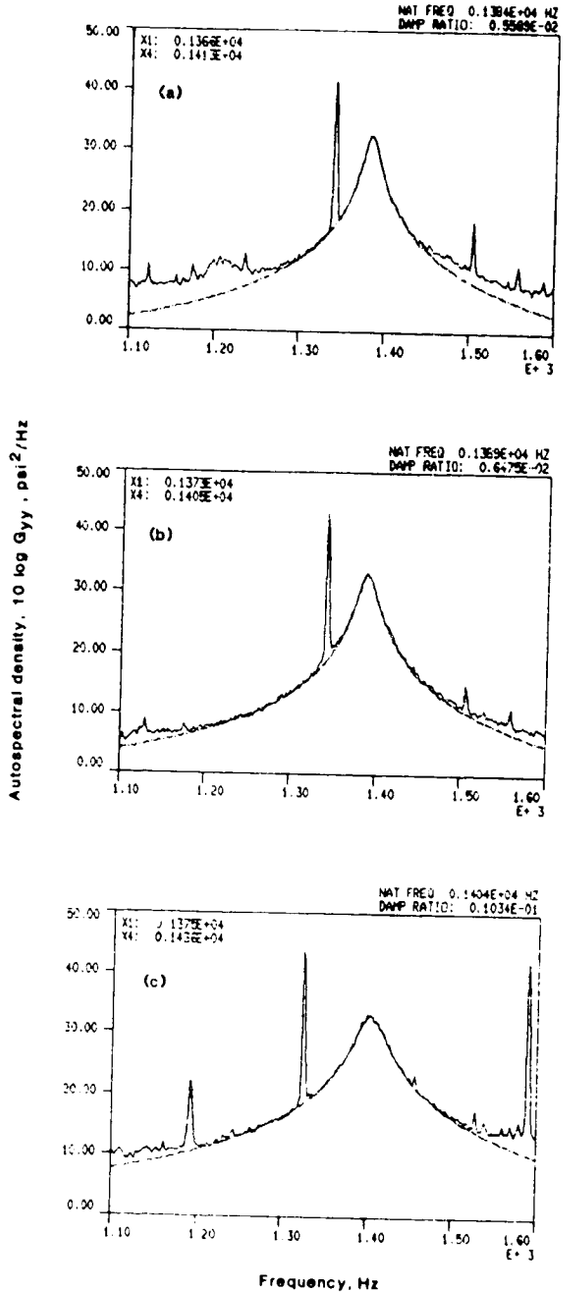

Figure A.3 - Rotor three first bending mode measured with gage 23 at design equivalent speed with maximum efficiency IGV-stator setting angles. Inlet total pressure/standard pressure (a) 0.366, (b) 0.505, (c) 0.761.

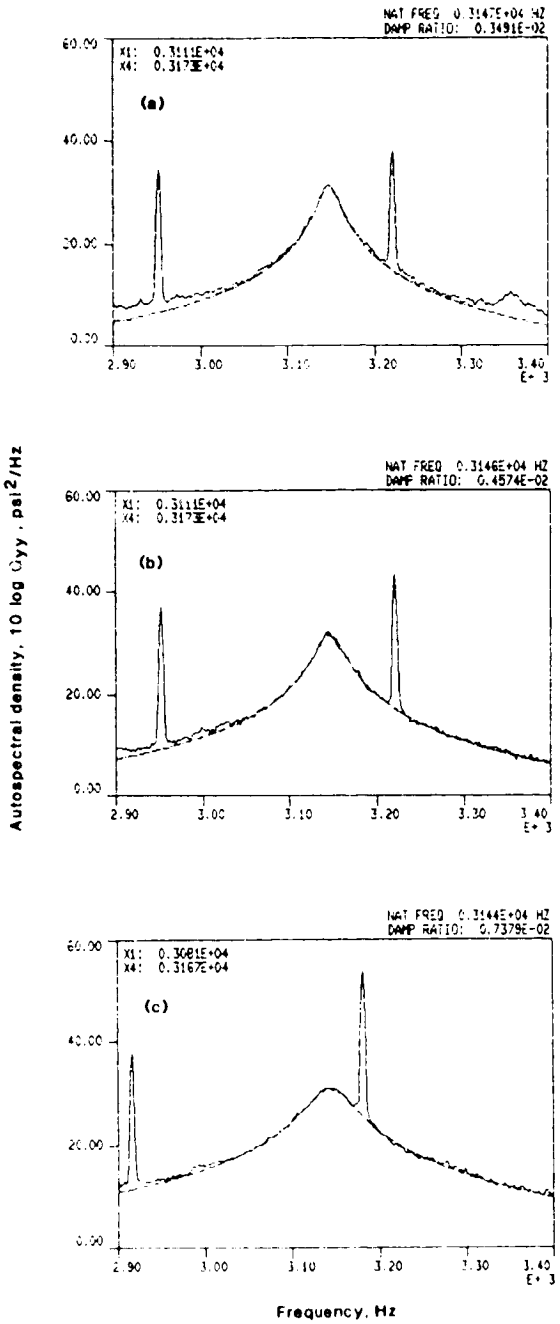

Figure A.4 - Rotor three first torsion mode measured with gage 17 at design equivalent speed with maximum efficiency IGV-stator setting angles. Inlet total pressure/standard pressure (a) 0.366, (b) 0.505, (c) 0.760.

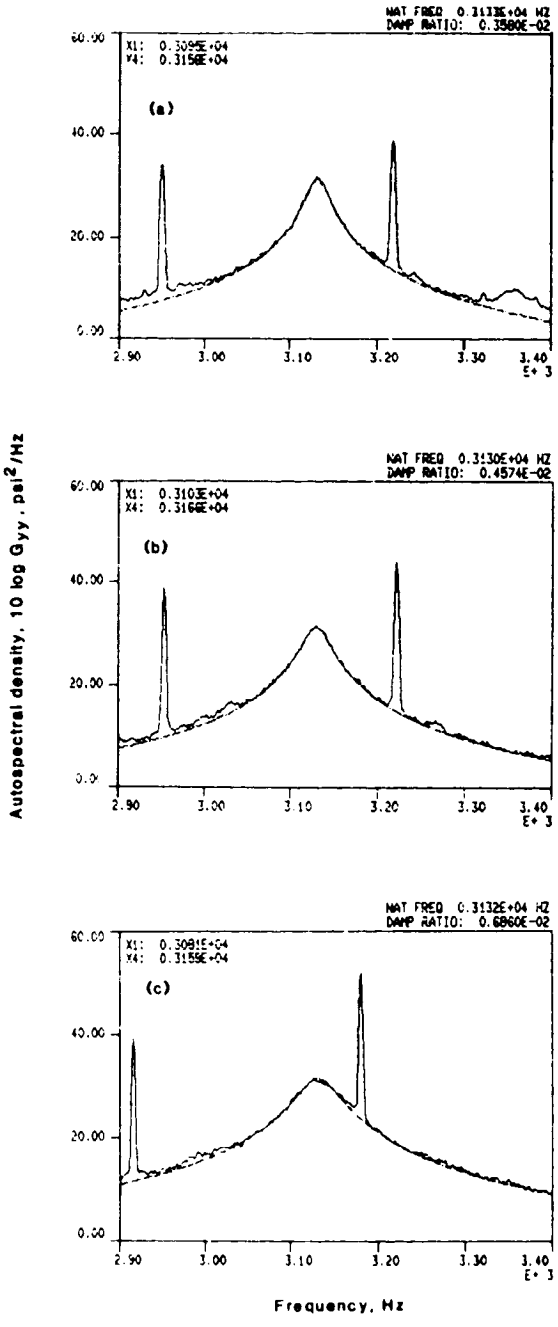

Figure A.5 - Rotor three first torsion mode measured with gage 19 at design equivalent speed with maximum efficiency IGV-stator setting angles. Inlet total pressure/standard pressure (a) 0.366, (b) 0.505, (c) 0.760.

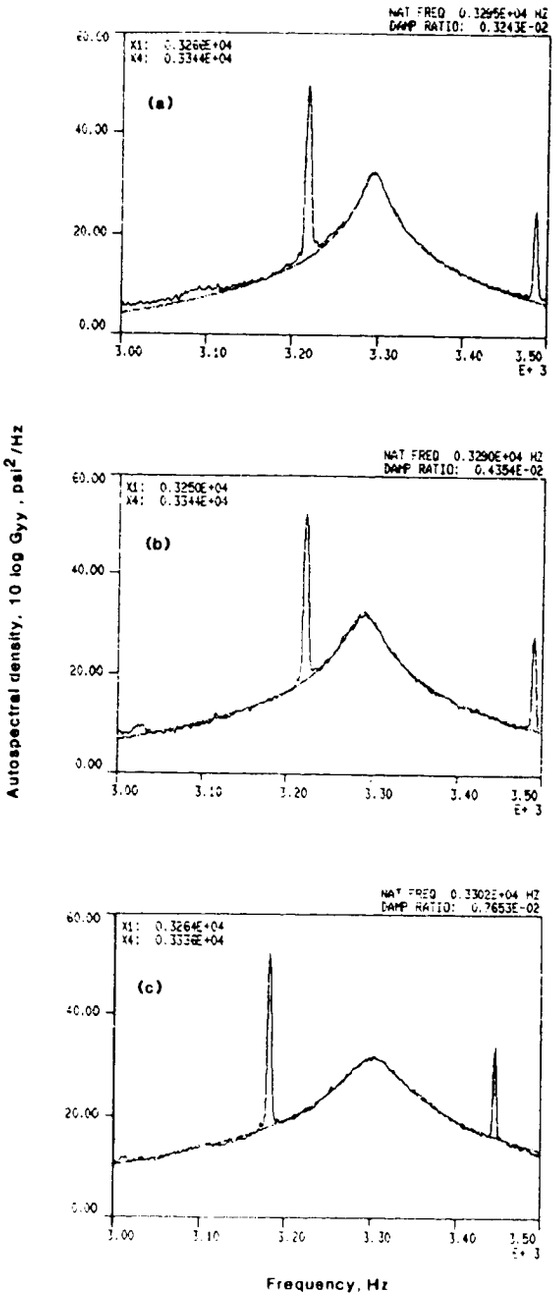

Figure A.6 - Rotor three first torsion mode measured with gage 23 at design equivalent speed with maximum efficiency IGV-stator setting angles. Inlet total pressure/standard pressure (a) 0.366, (b) 0.505, (c) 0.761.

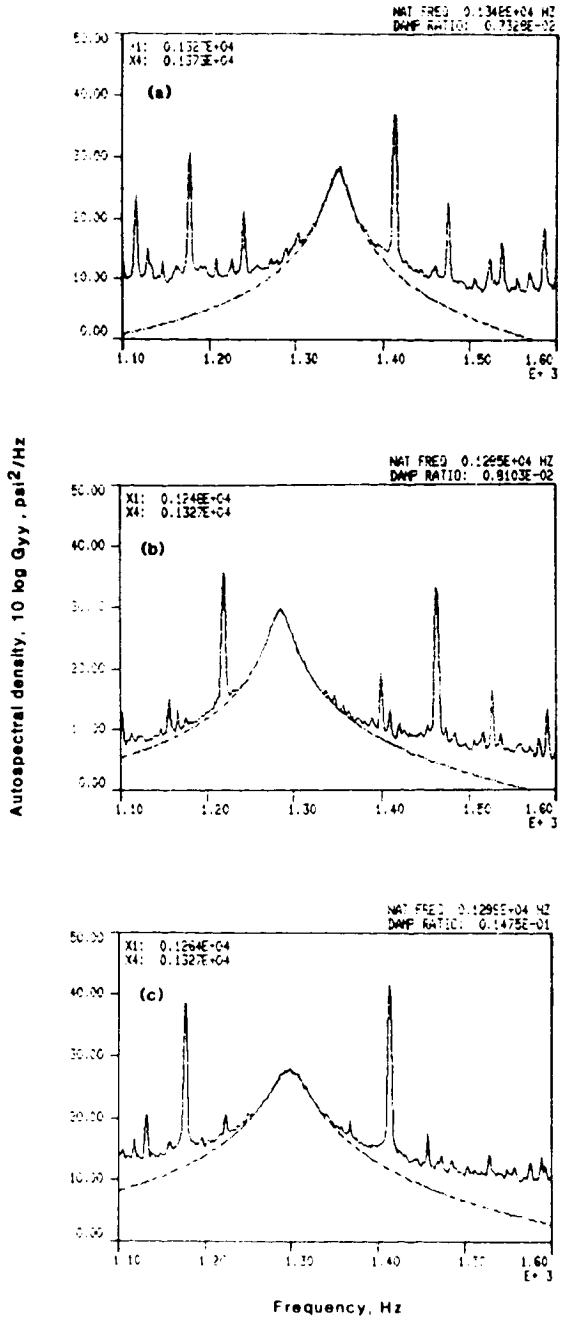

Figure A.7 - Rotor three first bending mode measured with gage 17 at 90 percent design equivalent speed with design IGV-stator setting angles. Inlet total pressure/standard pressure (a) 0.349, (b) 0.503, (c) 0.754.

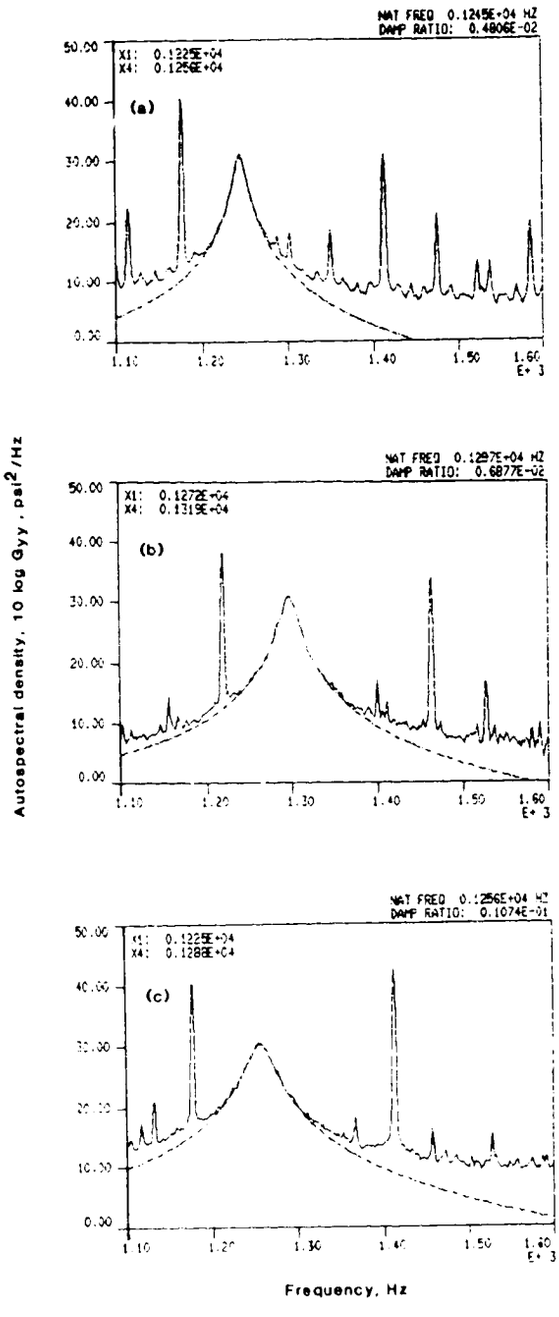

Figure A.8 - Rotor three first bending mode measured with gage 19 at 90 percent design equivalent speed with design IGV-stator setting angles Inlet total pressure/standard pressure (a) 0.349, (b) 0.503, (c) 0.754.

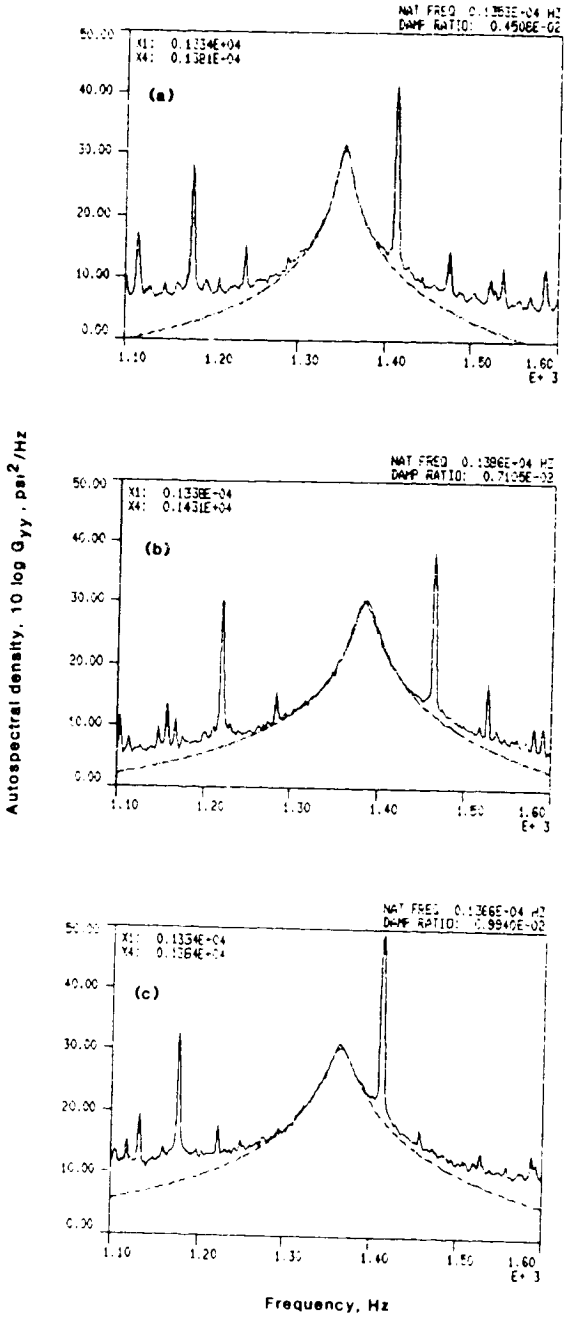

Figure A.9 - Rotor three first bending mode measured with gage 23 at 90 percent design equivalent speed with design IGV-stator setting angles. Inlet total pressure/standard pressure (a) 0.349, (b) 0.504, (c) 0.754.

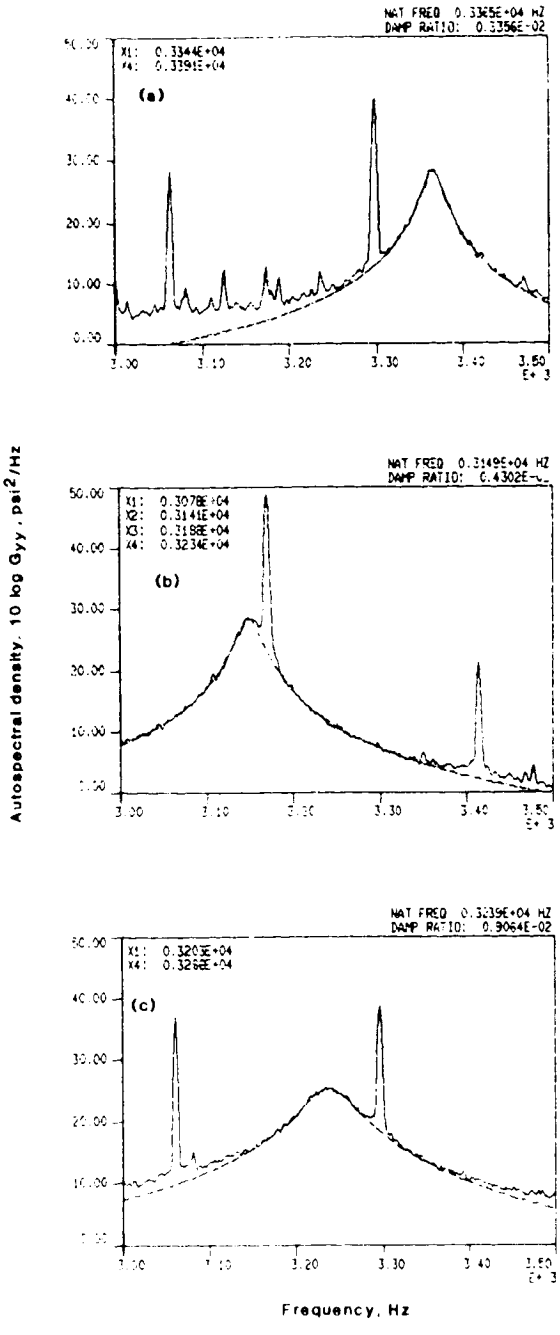

Figure A.10 - Rotor three first torsion mode measured with gage 17 at 90 percent design equivalent speed with design IGV-stator setting angles. Inlet total pressure/standard pressure (a) 0.349, (b) 0.503, (c) 0.754.

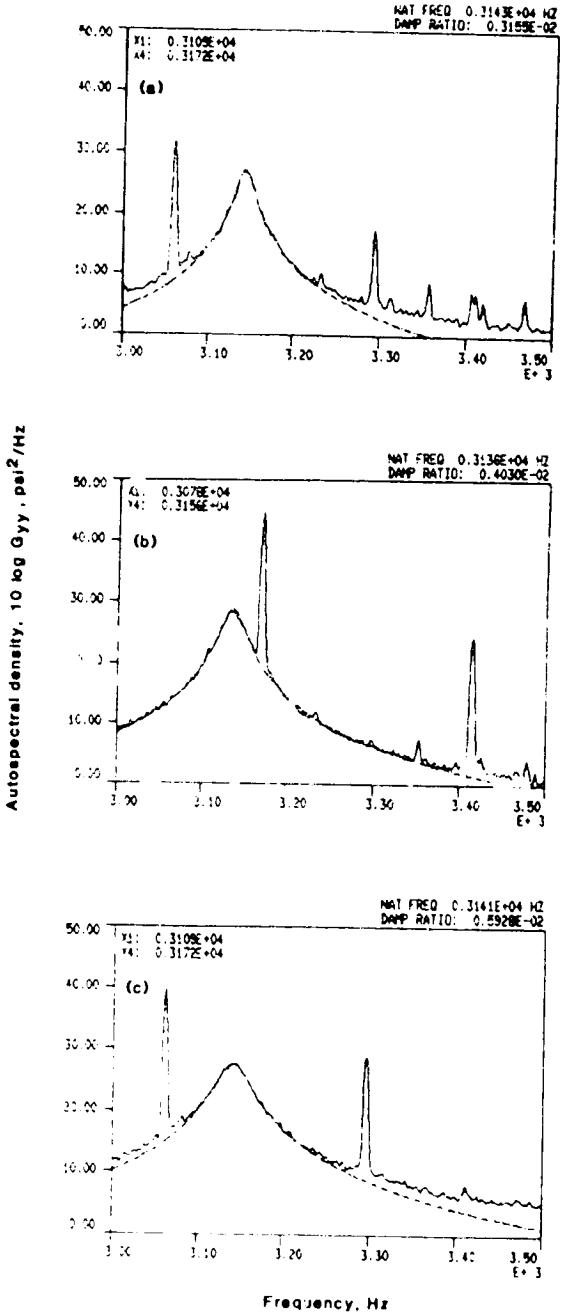

Figure A.11 - Rotor three first torsion mode measured with gage 19 at 90 percent design equivalent speed with design IGV-stator setting angles. Inlet total pressure/standard pressure (a) 0.349, (b) 0.503, (c) 0.754.

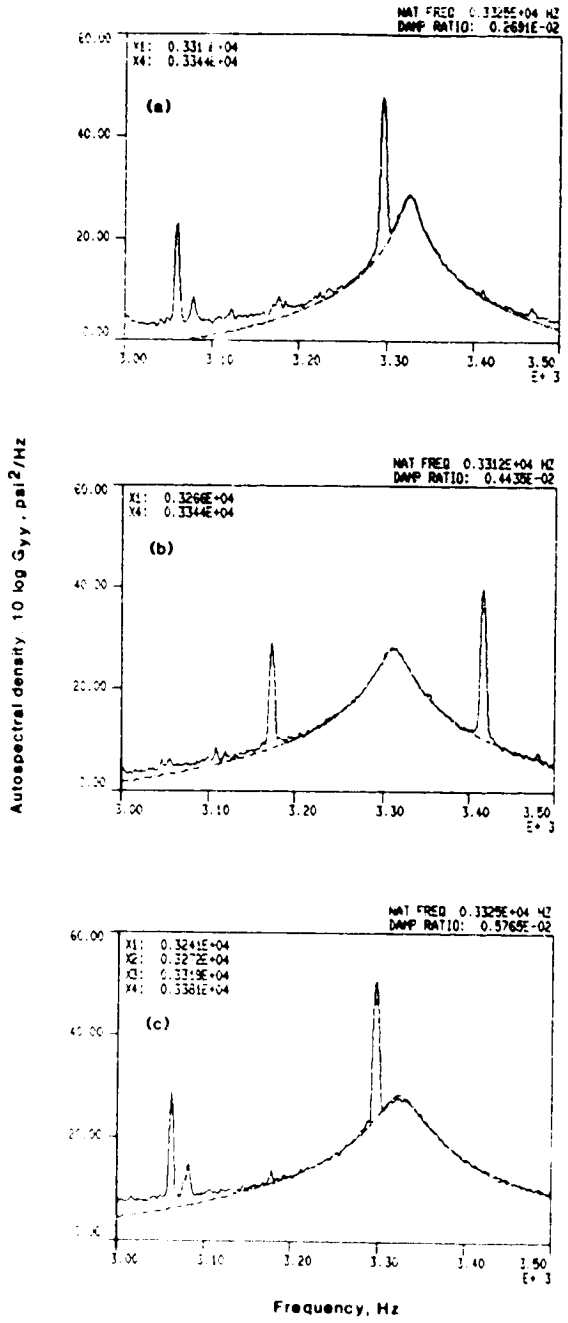

Figure A.12 - Rotor three first torsion mode measured with gage 23 at 90 percent design equivalent speed with design IGV-stator setting angles. Inlet total pressure/standard pressure (a) 0.349, (b) 0.504, (c) 0.754.

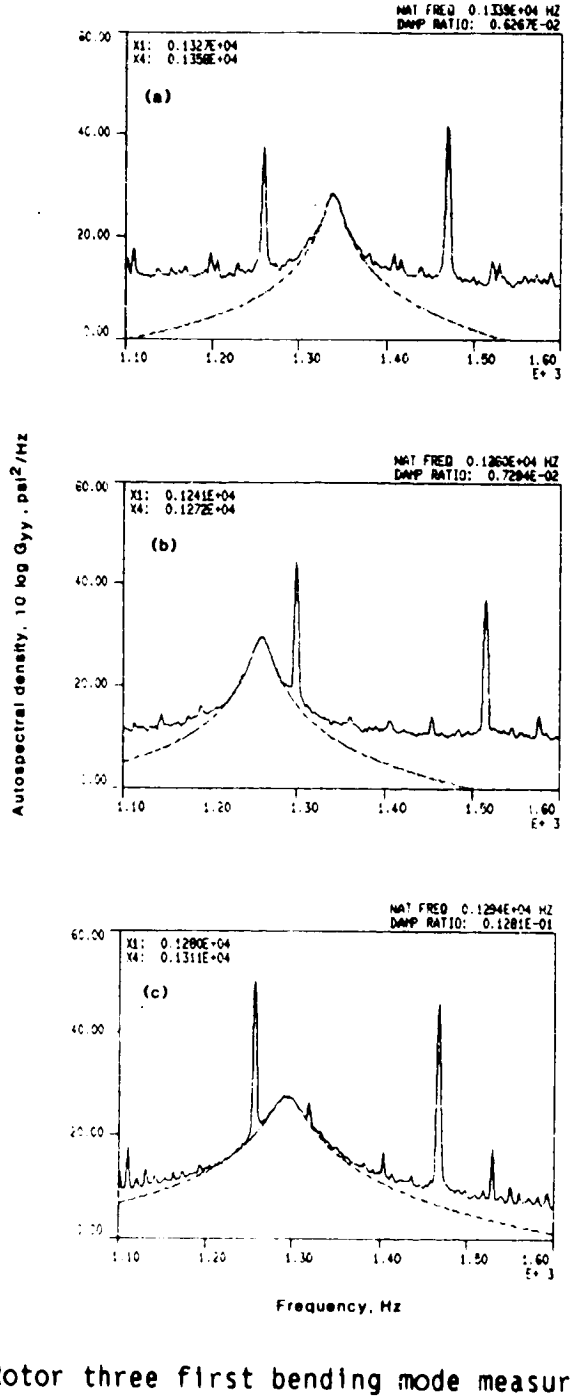

Figure A.13 - Rotor three first bending mode measured with gage 17 at 80 percent design equivalent speed with design IGV-stator setting angles. Inlet total pressure/standard pressure (a) 0.349, (b) 0.509, (c) 0.825.

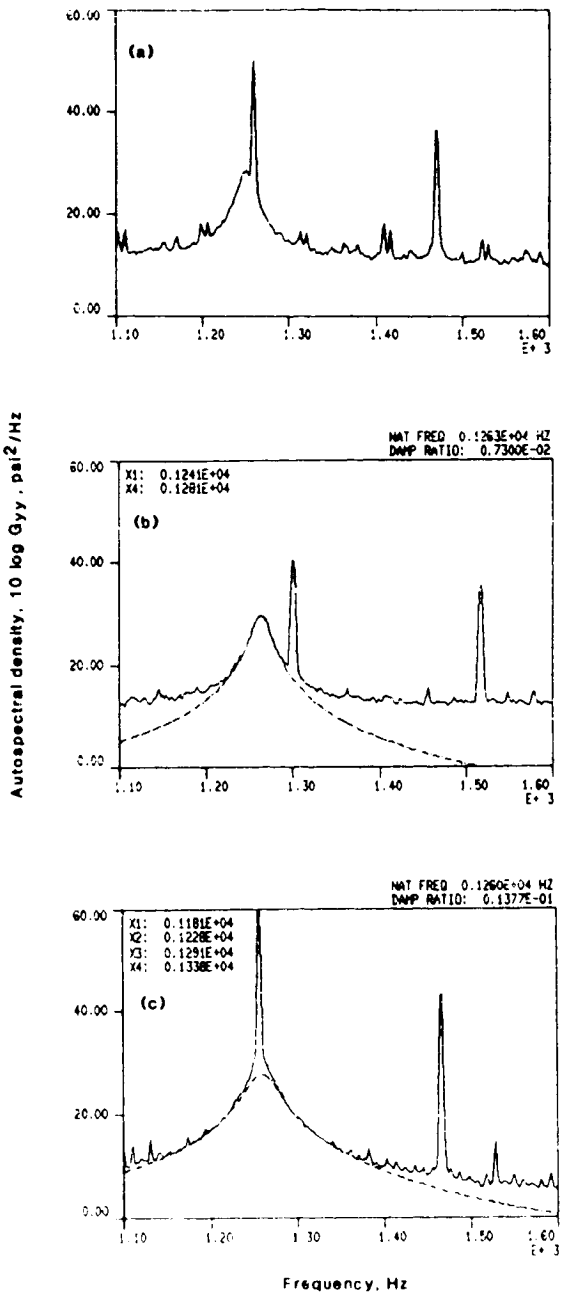

Figure A.14 - Rotor three first bending mode measured with gage 19 at 80 percent design equivalent speed with design IGV-stator setting angles. Inlet total pressure/standard pressure (a) 0.349, (b) 0.509, (c) 0.825.

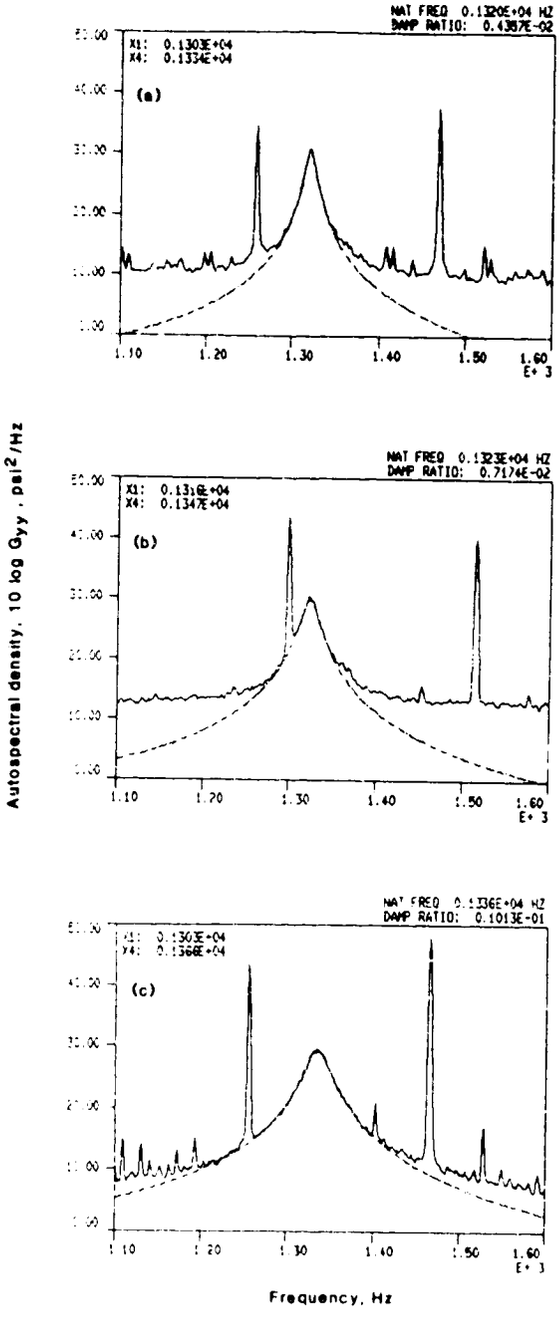

Figure A.15 - Rotor three first bending mode measured with gage 23 at 80 percent design equivalent speed with design IGV-stator setting angles. Inlet total pressure/standard pressure (a) 0.349, (b) 0.509, (c) 0.825.

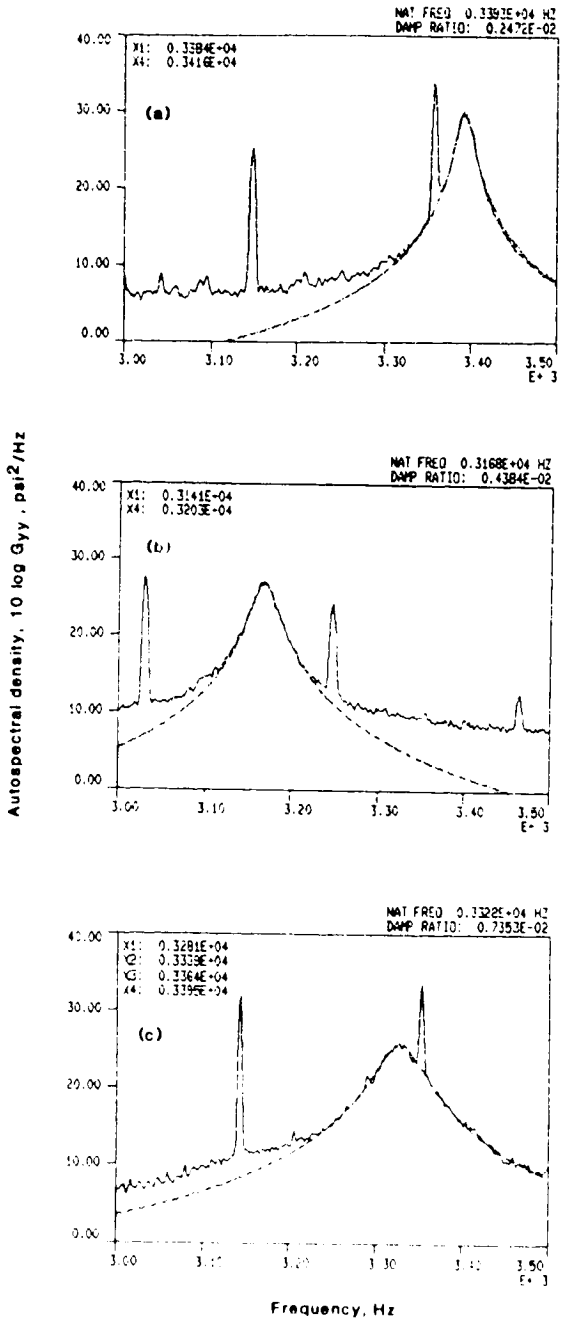

Figure A.16 - Rotor three first torsion mode measured with gage 17 at 80 percent design equivalent speed with design IGV-stator setting angles. Inlet total pressure/standard pressure (a) 0.349, (b) 0.509, (c) 0.825.

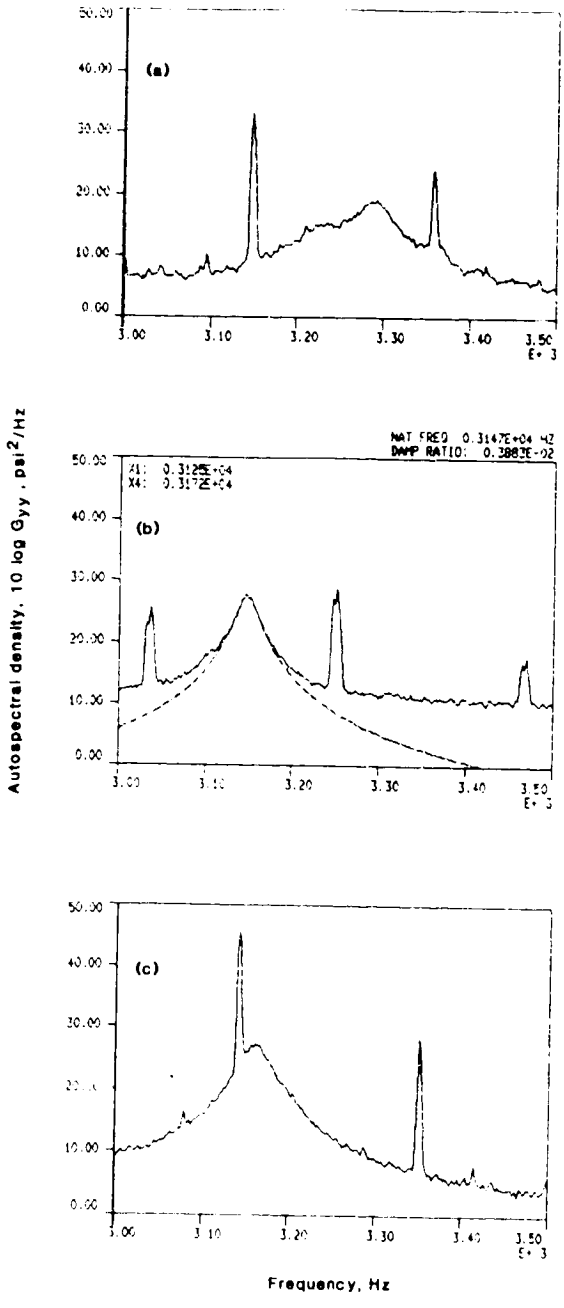

Figure A.17 - Rotor three first torsion mode measured with gage 19 at 80 percent design equivalent speed with design IGV-stator setting angles. Inlet total pressure/standard pressure (a) 0.349, (b) 0.509, (c) 0.825.

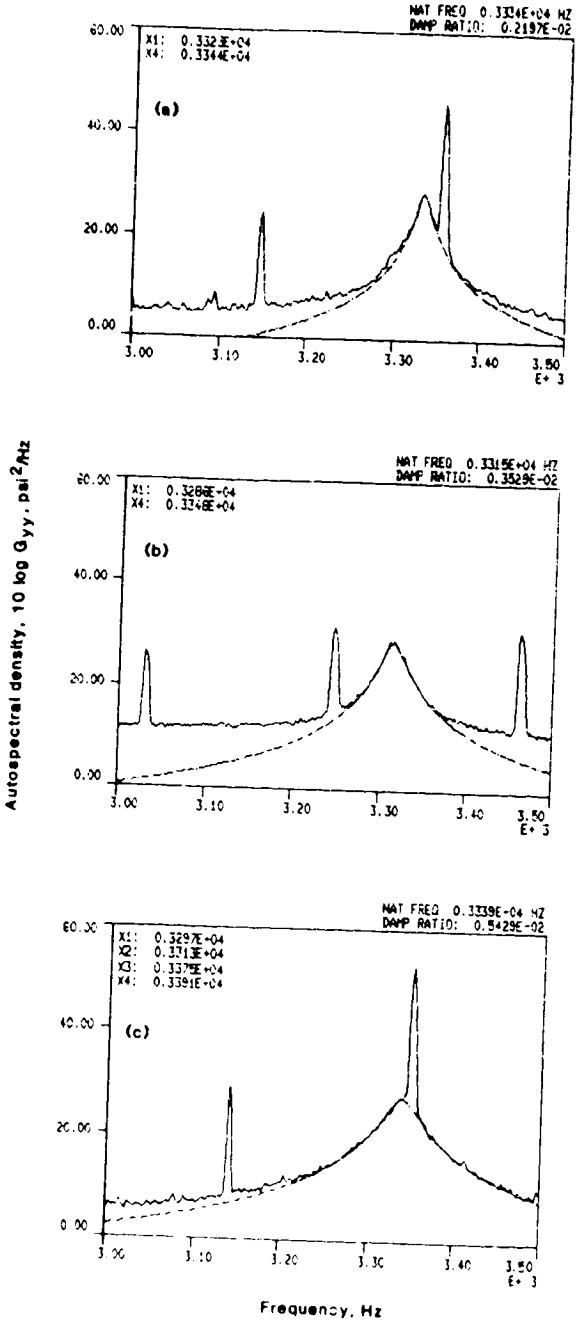

Figure A.18 - Rotor three first torsion mode measured with gage 23 at 80 percent design equivalent speed with design IGV-stator setting angles. Inlet total pressure/standard pressure (a) 0.349, (b) 0.509, (c) 0.825.

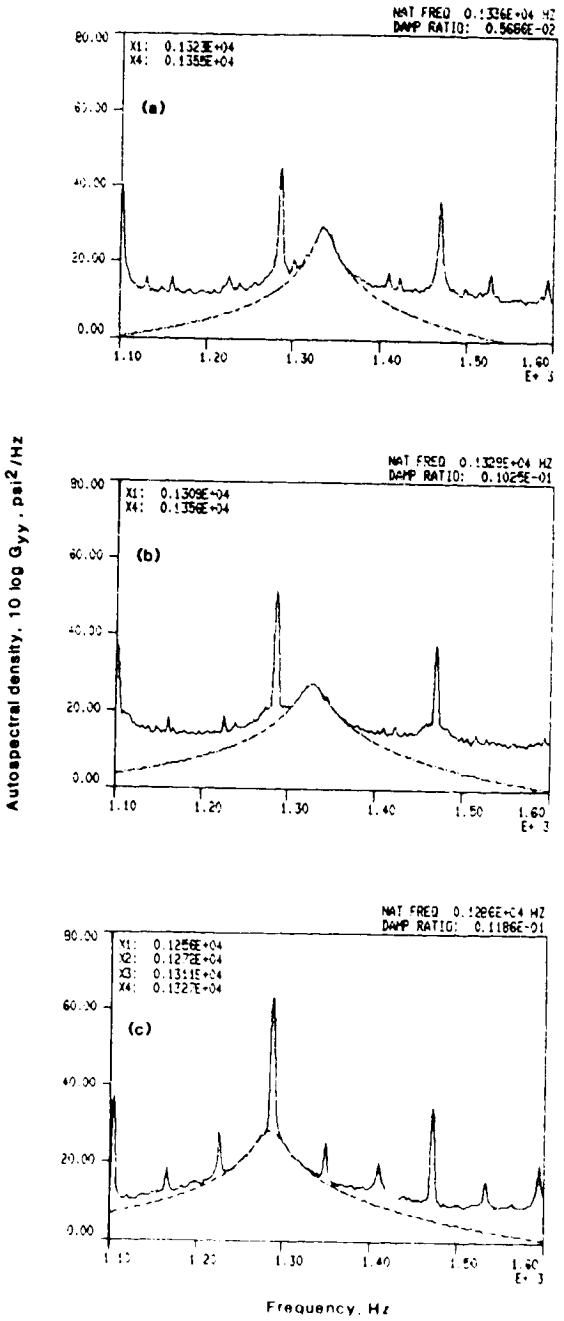

Figure A.19 - Rotor three first bending mode measured with gage 17 at 70 percent desi equivalent speed with design IGV-stator setting angles. Ini total pressure/standard pressure (a) 0.355, (b) 0.506, (c) 0.864.

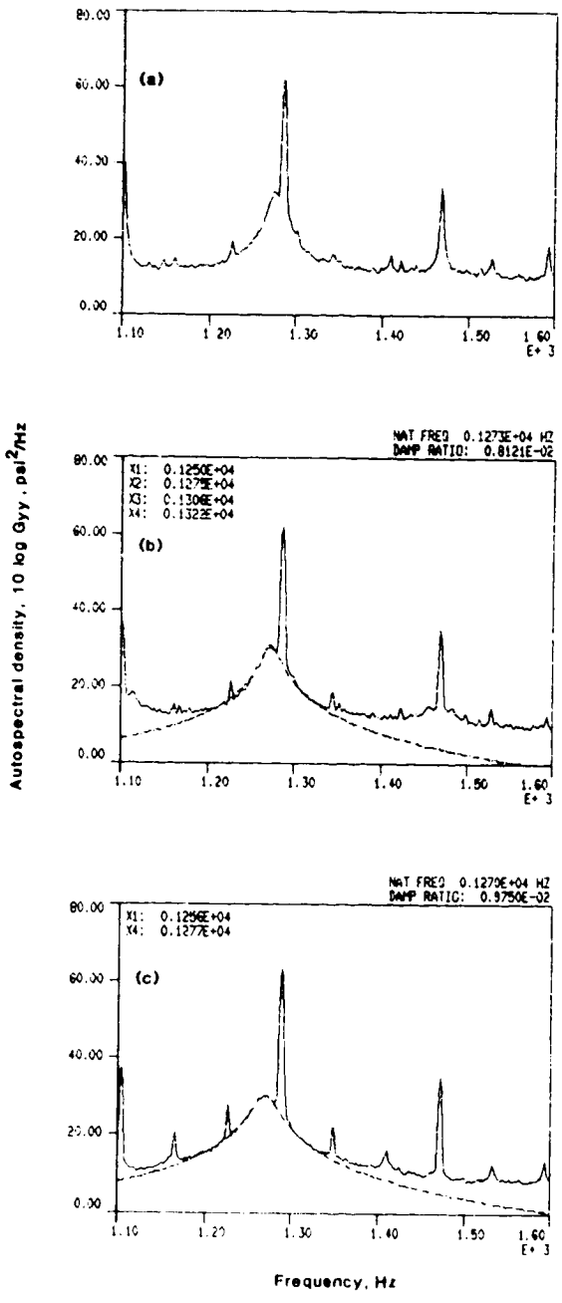

Figure A.20 - Rotor three first bending mode measured with gage 19 at 70 percent design equivalent speed with design IGV-stator setting angles. Inlet total pressure/standard pressure (a) 0.355, (b) 0.506, (c) 0.864.

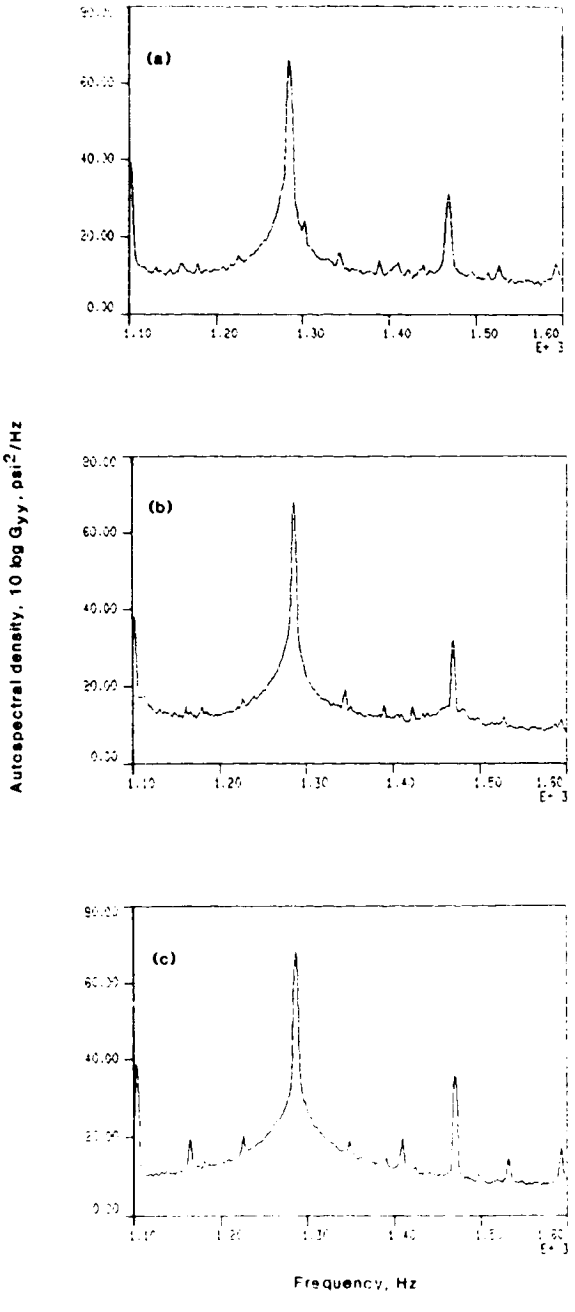

Figure A.21 - Rotor three first bending mode measured with gage 23 at 70 percent design equivalent speed with design IGV-stator setting angles. Inlet total pressure/standard pressure (a) 0.355, (b) 0.506, (c) 0.864.

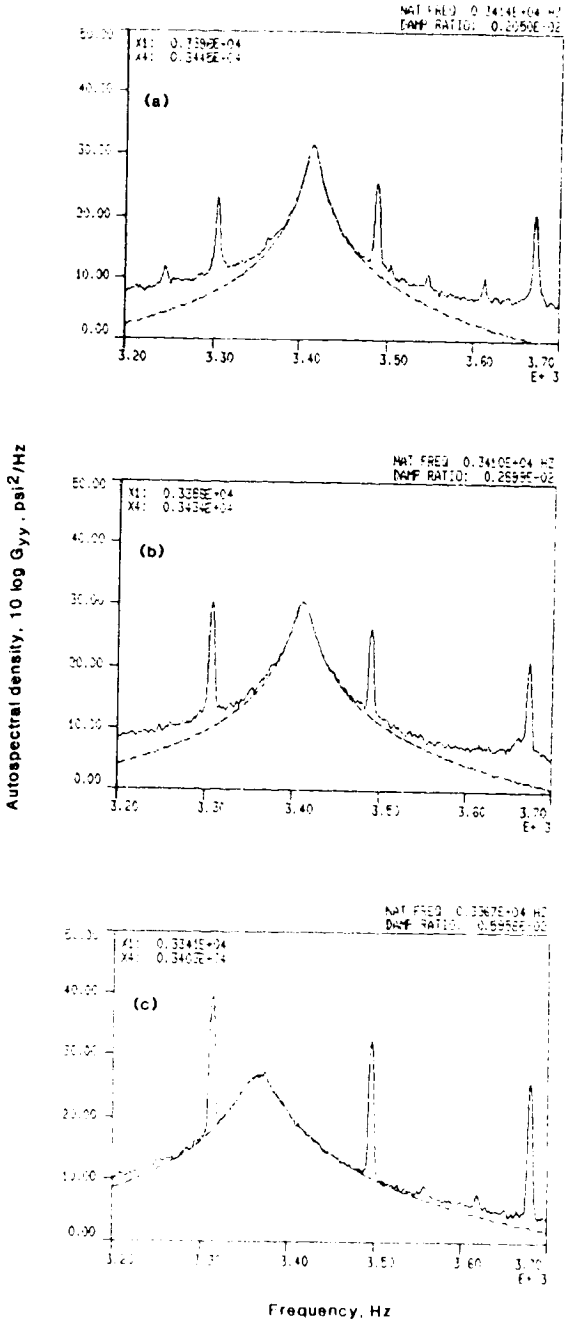

Figure A.22 - Rotor three first torsion mode measured with gage 17 at 70 percent design equivalent speed with design IGV-stator setting angles. Inlet total pressure/standard pressure (a) 0.355, (b) 0.506, (c) 0.864.

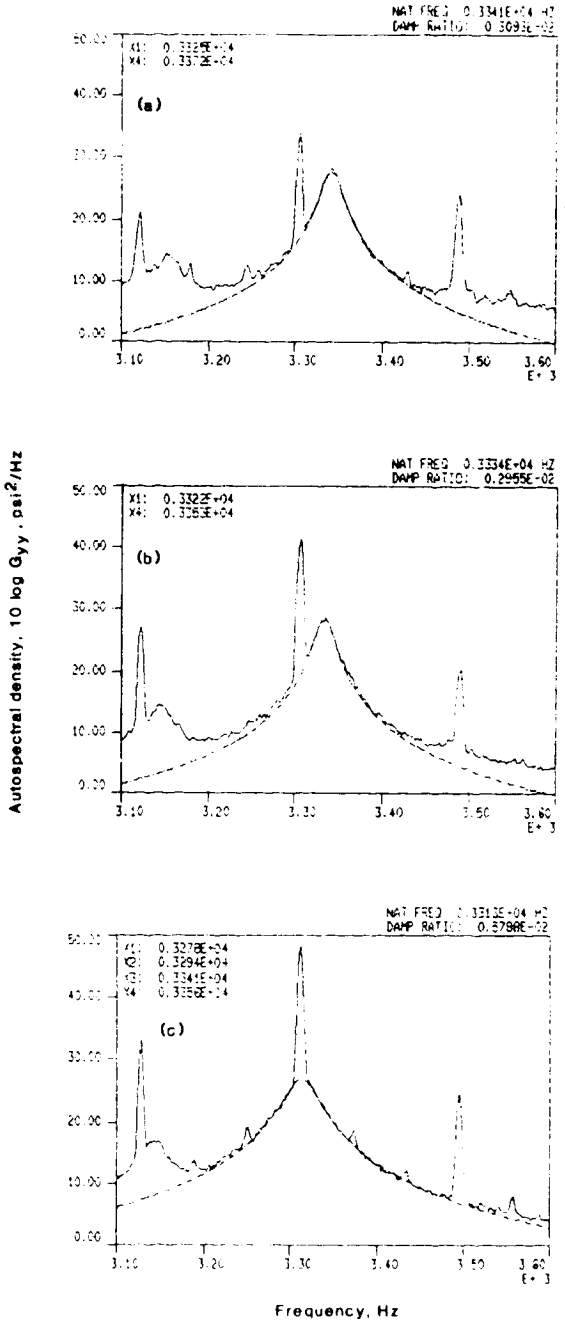

Figure A.23 - Rotor three first torsion mode measured with gage 19 at 70 percent design equivalent speed with design IGV-stator setting angles. Inlet total pressure/standard pressure (a) 0.355, (b) 0.506, (c) 0.864.

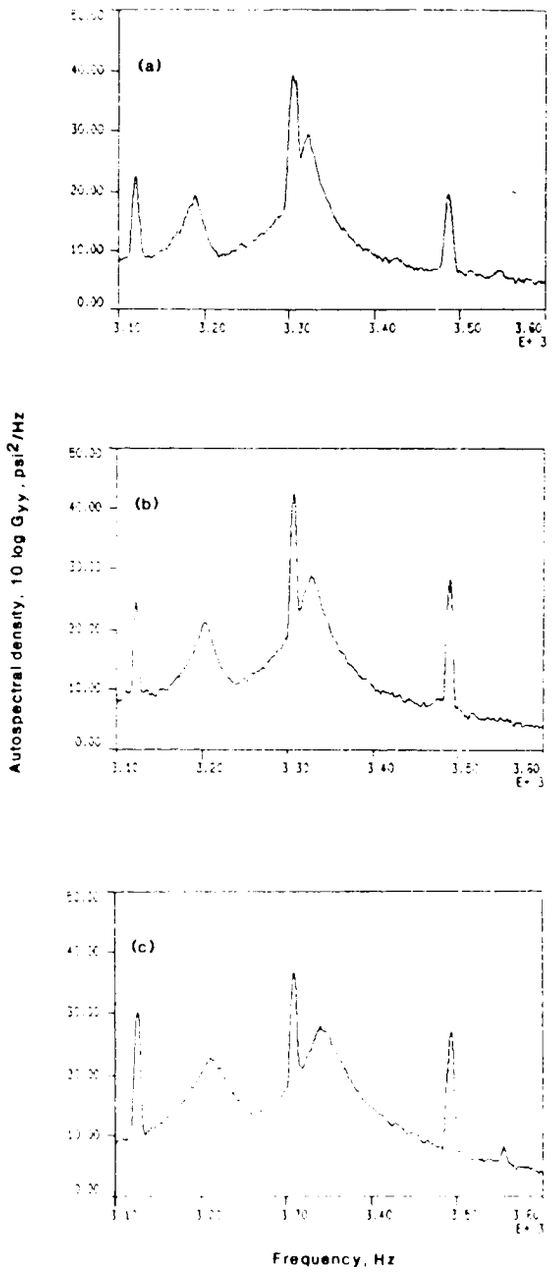

Figure A.24 - Rotor three first torsion mode measured with gage 23 at 70 percent design equivalent speed with design IGV-stator setting angles. Inlet total pressure/standard pressure (a) 0.355, (b) 0.506, (c) 0.864.

NASA
National Aeronautics and Space Administration

Report Documentation Page

1. Report No.	2. Government Accession No.	3. Recipient's Catalog No.
NASA TM-100953		

4. Title and Subtitle	5. Report Date
Experimental Determination of Aerodynamic Damping in a Three-Stage Transonic Axial-Flow Compressor	August 1988
	6. Performing Organization Code

7. Author(s)	8. Performing Organization Report No.
Frederick A. Newman	E-4267
	10. Work Unit No.
	505-05-11

9. Performing Organization Name and Address	11. Contract or Grant No.
National Aeronautics and Space Administration Lewis Research Center Cleveland, Ohio 44135-3191	
	13. Type of Report and Period Covered
12. Sponsoring Agency Name and Address	Technical Memorandum
National Aeronautics and Space Administration Washington, D.C. 20546-0001	14. Sponsoring Agency Code

15. Supplementary Notes

This report was a thesis submitted in partial fulfillment of the requirements for the degree of Master of Science to the Department of Mechanical and Aerospace Engineering, Case Western Reserve University, Cleveland, Ohio, in August 1988.

16. Abstract

Rotor blade aerodynamic damping is experimentally determined in a three-stage transonic axial flow compressor having design aerodynamic performance goals of 4.5:1 pressure ratio and 65.5 lbm/sec weight flow. The combined damping associated with each mode is determined by a least squares fit of a single degree of freedom system transfer function to the nonsynchronous portion of the rotor blade strain gage output power spectra. The combined damping consists of the aerodynamic damping and the structural and mechanical damping. The aerodynamic damping varies linearly with the inlet total pressure for a given equivalent speed, equivalent mass flow and pressure ratio while the structural and mechanical damping is assumed to be constant. The combined damping is determined at three inlet total pressure levels to obtain the aerodynamic damping. The third stage rotor blade aerodynamic damping is presented and discussed for 70, 80, 90, and 100 percent design equivalent speed. The compressor overall performance and experimental Campbell diagrams for the third stage rotor blade row are also presented.

17. Key Words (Suggested by Author(s))	18. Distribution Statement
Unsteady aerodynamics Aerodynamic damping Multistage transonic axial compressor Rotor blade vibration	Unclassified - Unlimited Subject Category 07

19. Security Classif. (of this report)	20. Security Classif. (of this page)	21. No of pages	22. Price*
Unclassified	Unclassified	112	A06

NASA FORM 1626 OCT 86

*For sale by the National Technical Information Service, Springfield, Virginia 22161

END

DATE

FILMED

OCT 11 1988